Geochemical Perspectives Letters

Sulfur loss from subducted altered oceanic crust and implications for mantle oxidation

J.B. Walters[1,2*], A.M. Cruz-Uribe[1], H.R. Marschall[2,3]

doi: 10.7185/geochemlet.2011

Abstract

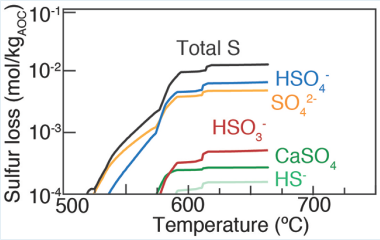

Oxygen fugacity (fO_2) is a controlling factor of the physics of Earth's mantle; however, the mechanisms driving spatial and secular changes in fO_2 associated with convergent margins are highly debated. We present new thermodynamic models and petrographic observations to predict that oxidised sulfur species are produced during the subduction of altered oceanic crust. Sulfur loss from the subducting slab is a function of the protolith $Fe^{3+}/\Sigma Fe$ ratio and subduction zone thermal structure, with elevated sulfur fluxes predicted for oxidised slabs in cold subduction zones. We also predict bi-modal release of sulfur-bearing fluids, with a low volume shallow flux of reduced sulfur followed by an enhanced deep flux of sulfate and sulfite species, consistent with oxidised arc magmas and associated copper porphyry deposits. The variable SO_x release predicted by our models both across and among active margins may introduce fO_2 heterogeneity to the upper mantle.

Received 27 September 2019 | Accepted 26 February 2020 | Published 2 April 2020

Introduction

Subduction may influence the oxygen fugacity (fO_2) of the mantle and mantle-derived magmas through the introduction of hydrated and oxidised altered oceanic crust (AOC, Fig. 1; Evans, 2012). Mantle fO_2 can regulate mantle rheology and density through changes in mineralogy; for example, the H_2O content of nominally anhydrous minerals is a function of fO_2 (McCammon *et al.*, 2004). As a result, secular changes in mantle fO_2 induced by plate tectonics may drive variations in mantle circulation (Mackwell, 2008). However, the link between redox sensitive elements in subducting slabs and mantle fO_2 at subduction zones remains elusive.

Mounting evidence suggests that mantle fO_2 evolves in response to a transfer of oxidised slab components. For example, peridotite xenoliths from Mexico record fO_2 conditions 1.5–2.4 log units above the quartz-fayalite-magnetite (QFM) buffer (Blatter and Carmichael, 1998), whereas mid-ocean ridge peridotite overlaps with QFM (Birner *et al.*, 2018). Similarly, arc magmas are oxidised relative to mid-ocean ridge basalts (MORB; Kelley and Cottrell, 2009, 2012; Cottrell and Kelley, 2011; Brounce *et al.*, 2014). The $Fe^{3+}/\Sigma Fe$ ratios of arc magmas positively correlate with geochemical indicators of material addition from the slab to the magma sources, such as Ba/La ratios (Kelley and Cottrell, 2009); therefore, elevated mantle fO_2 along convergent margins is both spatially and chemically linked to the subducting slab.

Such a link may require the transfer of redox sensitive elements from slab lithologies, which are oxidised relative to mantle peridotite. Early studies hypothesised the introduction of slab Fe^{3+} (*e.g.*, Lecuyer and Ricard, 1999); however, the solubility of Fe^{3+} in hydrous fluids is low (Mungall, 2002). Instead, volatiles likely play a more important role (Evans, 2012). Of these, only H, C, and S potentially occur in sufficient abundance to influence the redox state of the mantle. Sulfur and carbon are fluid mobile, exhibit an eight electron range in oxidation states, are subducted at global rates on the order of 10^{12} mol/yr, and may act as important vectors for transferring oxidation state (Evans, 2012). Significant work has focused on decarbonation during subduction, whereas sulfur loss remains less explored. This is despite the fact that the transition from S^{2-} to SO_4^{2-} occurs at more oxidising conditions relative to the C-CO_2 transition (Fig. S-1). Oxidised carbon is stable at normal upper mantle *P–T–*fO_2; therefore, slab-derived CO_2 fluxes are unable to initiate Fe oxidising reactions in the mantle wedge (see Supplementary Information S-2). In contrast, a flux of oxidised sulfur may raise log(fO_2) of the subarc mantle to ~QFM + 2, consistent with the range commonly observed in subarc mantle xenoliths (*e.g.*, Blatter and Carmichael, 1998). Sulfur thus remains the most powerful oxidising agent in subduction zones.

Recent studies have favoured either reduced (H_2S, HS^-) or oxidised (SO_4^{2-}) sulfur species in slab fluids, with the potential to reduce or oxidise the subarc mantle (*e.g.*, Evans

1. School of Earth and Climate Sciences, University of Maine, 5790 Bryand Global Sciences Center, Orono, Maine 04469, USA
2. Institut für Geowissenschaften, Goethe-Universität Frankfurt, Altenhöferallee 1, 60438 Frankfurt am Main, Germany
3. Department of Geology and Geophysics, Woods Hole Oceanographic Institution, Woods Hole, MA, USA
* Corresponding author (email: jesse.walters@maine.edu)

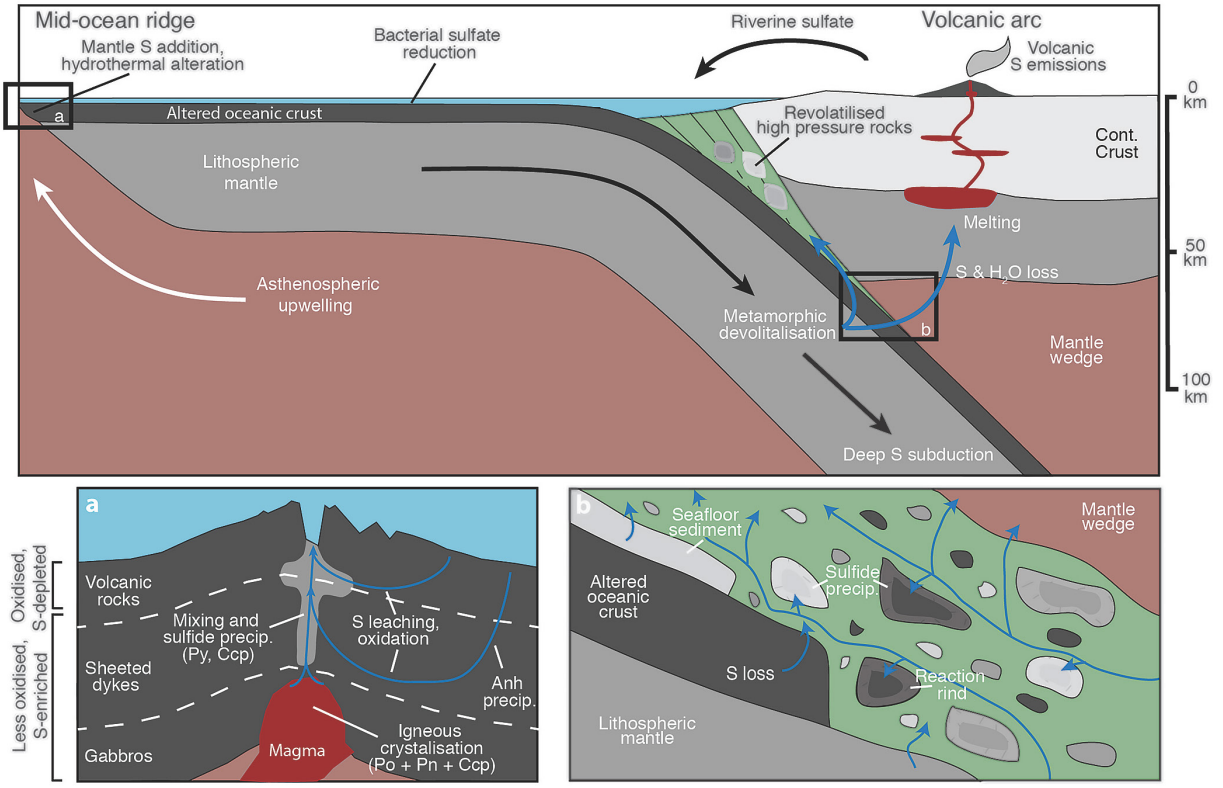

Figure 1 Schematic diagram showing the broader subduction zone system. Sulfur is introduced to the oceanic crust during crystallisation and hydrothermal circulation. **(a)** Magmatic sulfides react to form pyrite ± chalcopyrite and iron is oxidised (see Supplementary Information S-1). Sulfur is later extracted during metamorphic devolatilisation. **(b)** Sulfides precipitate in reaction rinds formed upon exhumation of metamorphic rocks along the slab mantle interface, while the remaining sulfur infiltrates the overlying subarc mantle.

et al., 2014; Tomkins and Evans, 2015; Walters *et al.*, 2019). We address this discrepancy through thermodynamic modelling using the Gibbs free energy minimisation software Perple_X (Connolly, 2005) to predict sulfur speciation in AOC-derived fluids (see Supplementary Information S-3). This enables us to assess the potential of sulfur to influence mantle and arc fO_2 as a function of slab composition and subduction zone thermal structure. We predict that oxidised sulfur species are dominant in slab fluids at eclogite facies conditions and may oxidise arc magmas and the subarc mantle.

Squeezing Sulfur from the Slab

Metamorphic assemblages predicted over a *P–T* range of 1.5–3.5 GPa and 500–800 °C for average AOC (Fig. 2) show a change from reduced to oxidised sulfur species with increasing depth. Sulfide and sulfate minerals comprise <0.5 vol. % of the rocks, consistent with their low abundance in most high pressure rocks. Pyrrhotite is stable below 1.8 GPa and <680 °C, above which it is replaced by pyrite. Pyrite is converted to anhydrite with increasing *P–T* (*e.g.*, >2.3 GPa at 650 °C). Anhydrite is the only sulfur phase at pressures above 2.8–3.3 GPa (Fig. 2). Sulfur oxidation is balanced by reduction of ferric iron, resulting in a decrease in $Fe^{3+}/\Sigma Fe$ from 0.28 to 0.13–0.17 (Fig. S-4) in the dehydrated slab residue (*i.e.* eclogite). Assemblages were also predicted for average MORB (Figs. S-6 and S-7) with an initial $Fe^{3+}/\Sigma Fe$ of 0.14. Although the compositions used here are averages, a comparison of AOC and MORB allows us to assess the degree to which alteration of the oceanic crust may influence sulfur loss. The sulfur oxidising reactions are shifted to higher pressures and $Fe^{3+}/\Sigma Fe$ is constant with depth in the MORB model (Fig. S-10), suggesting that prograde sulfur oxidation varies as a function of pre-subduction seafloor alteration.

Sulfur concentration and speciation in slab fluids vary as a function of subduction zone thermal structure, which we demonstrate by comparing open system models in which fluids are fractionated at each *P–T* step along contrasting geothermal gradients (D80; Syracuse *et al.*, 2010). The Honshu ('cold') and Cascadia ('hot') models for average AOC display some similarity: fluid compositions transition from H_2S–HS^- to HSO_4^-–HSO_3^- dominant as the anhydrite-in reaction is approached with depth. Similarly, sulfur concentrations increase with depth along both paths. In the Honshu model, dissolved sulfur concentrations increase from 2.3 mmol/kg HS^-, 0.1 mmol/kg H_2S, and 0.5 mmol/kg HSO_4^- at 2.4 GPa and 500 °C to 481 mmol/kg HSO_4^-, 51.6 mmol/kg HSO_3^-, and 93.1 mmol/kg SO_4^{2-} at 2.5 GPa and 660 °C, the last *P-T* step before H_2O is exhausted (Fig. S-3). Concentration and speciation are similar in the high *P–T* region of the Cascadia model, yet at low *P–T*, H_2S and HS^- concentrations are two orders of magnitude greater than those in the Honshu model. In the Honshu model, sulfur loss is largely in the form of oxidised species during lawsonite breakdown at depths of 82 to 85 km (Fig. 3). In contrast, in the Cascadia model HS^- and H_2S dominate in the shallow region (<75 km), where nearly 60 % of the H_2O is lost (Fig. 3). We conclude from these models that hot subduction zones should exhibit shallow reduced and deep oxidised sulfur fluxes, whereas cold subduction zones will be dominated by the release of oxidised sulfur.

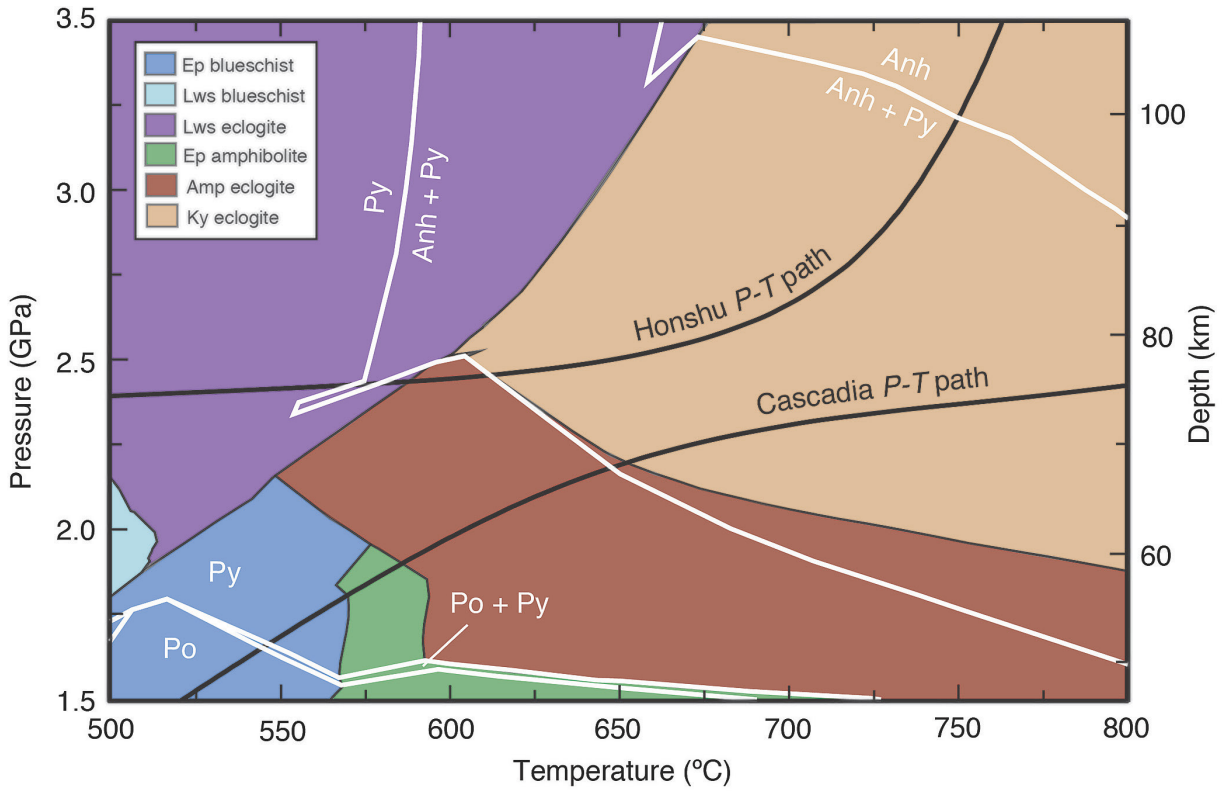

Figure 2 Closed system phase equilibrium modelling results utilising an average AOC composition from ODP hole 504B. The stability fields of common rock types are shaded (see key) and the stable solid sulfur phases are also highlighted. Honshu and Cascadia slab top *P-T* paths after Syracuse *et al.* (2010).

Oxidation of the oceanic crust enhances sulfur loss during subduction. Despite higher bulk rock sulfur and similar H_2O contents, sulfur fluid concentrations are an order of magnitude lower for MORB compared to AOC, and little oxidised sulfur is released (Figs. S-8 and S-9). These data suggest heterogenous sulfur loss within slabs, where the oxidised volcanic section of the crust is likely to exhibit greater sulfur loss than deeper lithologies (see Supplementary Information S-1). The AOC composition modelled in this study is an average of 6.6 Ma crust formed at a fast spreading centre. More pervasively altered oceanic crust formed at slow spreading centres may exhibit greater sulfur loss. However, these effects will be balanced by the degree to which sulfur is removed during oxidative alteration (see Supplementary Information S-1).

Our results are similar to those of Debret and Sverjensky (2017) for subducted serpentinite, where SO_x species were calculated to be released at 630–660 °C and 2.0 GPa. Similarly, Tomkins and Evans (2015) predicted dissolution of seafloor anhydrite in MORB to also occur over the blueschist-to-eclogite transition modelled here, potentially enhancing the oxidised nature of slab fluids released at these depths. In contrast, Li *et al.* (2020) predicted the release of reduced sulfur species during the subduction of mafic crust; however, the reduced nature of these fluids is a result of fixing fO_2 at QFM to QFM – 3 along the dehydration path. We suggest that these models are similar to our MORB models but are inconsistent with the elevated fO_2 of AOC.

The Exhumed Rock Record

Our models are consistent with the petrographic and isotopic record from exhumed high pressure rocks. Under regional metamorphic conditions, pyrite (S^-) is commonly replaced by pyrrhotite (S^{2-}) with increasing grade (*e.g.*, Tracy and Robinson, 1988). This mechanism was adopted in earlier models of pyrite behaviour during subduction of AOC (*e.g.*, Evans *et al.*, 2014). Such reactions, balanced by the oxidation of Fe^{2+} to Fe^{3+} in silicates or oxides, would produce H_2S in the presence of water during subduction (see review in Walters *et al.*, 2019). However, our data suggest that sulfur oxidation is balanced by iron reduction. The available $Fe^{3+}/\Sigma Fe$ data for high pressure minerals combined with mass balance constraints show that eclogites are reduced relative to blueschists and AOC (see Supplementary Information S-4). Iron reduction during the blueschist to eclogite facies transition in natural rocks has to be balanced by the oxidation of another element, and we suggest that sulfur is the only possible candidate and its prograde oxidation provides the mechanism.

Further support for our model comes from a recent isotopic study of sulfides precipitated from slab-derived fluids during the exhumation of high pressure rocks. The ~36 ‰ ($\delta^{34}S$) variation among metasomatic sulfides suggests that large fractionations (10–20 ‰) were induced by precipitation from oxidised sulfur-bearing slab fluids (Walters *et al.*, 2019). In addition, a recent study of Fe isotopes in high pressure garnet from Sifnos (Greece) suggests that lawsonite dehydration is accompanied by iron reduction in low temperature eclogites, likely due to a loss of SO_x species (Gerrits *et al.*, 2019). This is consistent with the predictions of our Honshu model.

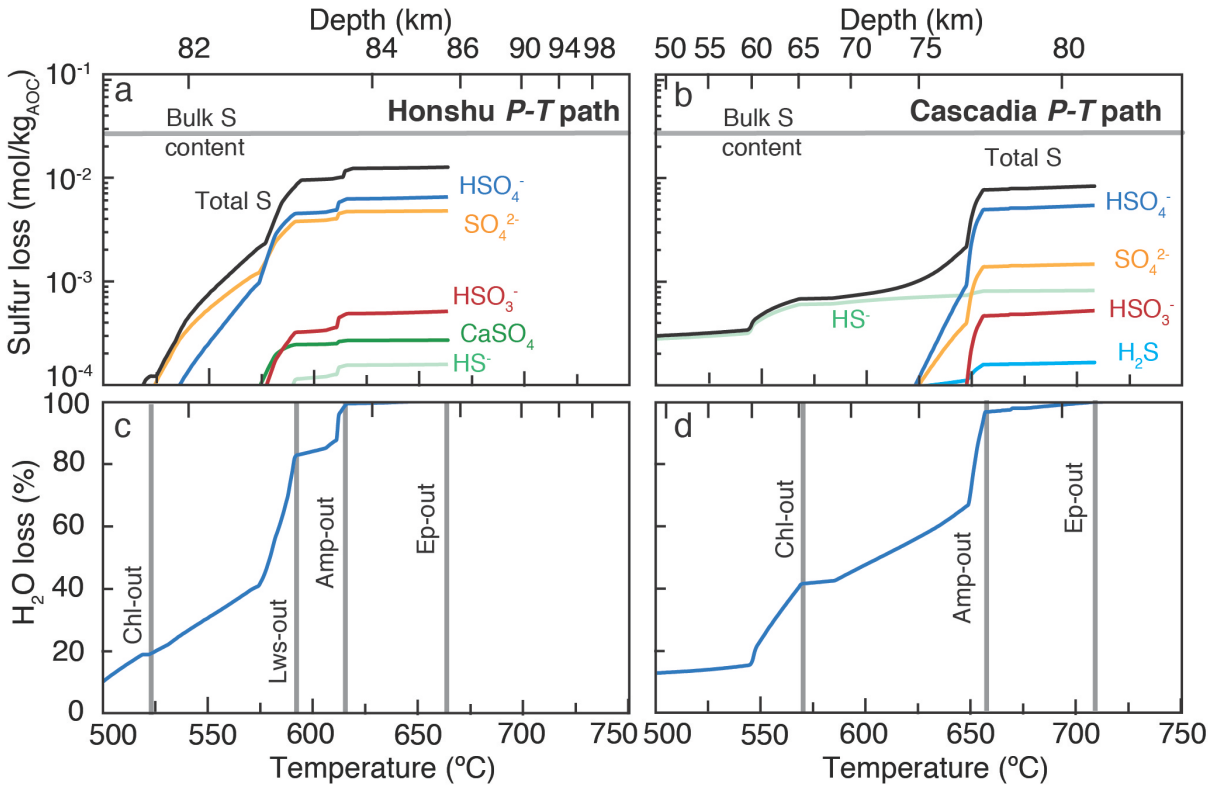

Figure 3 Cumulative sulfur **(a,b)** and fluid **(c,d)** loss diagrams for fluids fractionated along the Honshu and Cascadia *P-T* paths. Both temperature and corresponding slab top depth are plotted on the x-axis. Key dehydration reactions are shown for reference.

Sulfates are observed in fluid and solid inclusions in samples of subducted oceanic crust metamorphosed at relatively low pressures of 1.5–2.5 GPa (Frezzotti and Ferrando, 2015). This is consistent with our models for AOC, in which the sulfide-sulfate transition occurs at 2.0–2.5 GPa. In contrast, in more reduced (relative to AOC) eclogites embedded in subducted continental crust, sulfate-bearing inclusions are more commonly observed in rocks metamorphosed at pressures >3.0 GPa (Frezzotti and Ferrando, 2015). In agreement with these observations, we show that the sulfide-sulfate transition is shifted to >3.0 GPa in more reduced lithologies. However, there are limited observations of solid phase inclusions within subducted oceanic crust, and sample preparation with water during cutting, grinding, and polishing is likely to remove anhydrite.

Sulfides are a common trace phase found as inclusions in eclogitic minerals (Fig. 4a,b; see review in Walters *et al.*, 2019). Brown *et al.* (2014) observed prograde replacement of pyrrhotite-bearing inclusion assemblages by pyrite-bearing assemblages between 1.4-1.5 GPa and 450-500 °C and 1.9 GPa and 600 °C in New Caledonian HP rocks, consistent with the transformation of pyrrhotite to pyrite predicted by our models (Fig. 2). Matrix sulfides are commonly associated with hydrous metasomatic Fe^{3+}-rich phases, such as epidote, amphibole, and chlorite (Fig. 4c,d), consistent with fluid mediated sulfur reducing reactions.

The scarcity of peak eclogite facies matrix sulfides combined with remnant prograde sulfide inclusions suggests that sulfur loss is nearly complete following dehydration of AOC; however, our models predict that 55 to 75 % of the sulfur should remain in the slab (Fig. S-4). Dissolved NaCl dramatically increases anhydrite dissolution (Newton and Manning, 2004), but is not so far incorporated into our models. Therefore, SO_x concentrations are likely underpredicted in our models. Additional sulfur may also be mobilised by external fluids; however, fluids in these environments are likely channelised (*e.g.*, Zack and John, 2007), such that external fluids will not liberate significant amounts of sulfur from the majority of the subducted crust. Regardless, our current models likely provide a correct estimate of sulfur speciation and a minimum estimate for the total contribution from subducting AOC to the sulfur budget of arcs.

Oxidising the Arc

The migration of sulfate-bearing fluids from dehydrating AOC will oxidise the upper mantle. Upon contact with more reduced conditions of the mantle (~QFM), sulfides are expected to precipitate from slab fluids to oxidise Fe and hydrate the mantle wedge, a process which accounts for the QFM to QFM + 2 range in fO_2 reported for subarc peridotite xenoliths (see Supplementary Information S-2). Metasomatism is likely to strip slab fluids of their oxidising capability before reaching melt generation regions. Fluid loss is predicted in our models at depths (60 to 80 km) less than those of the slab top directly below many volcanic arcs (~100 km; Syracuse *et al.*, 2010). However, deflection of metasomatised mantle or mélange diapirs by corner flow may carry the oxidised mantle to the region of melt generation beneath the arc (Spandler and Pirard, 2013). Bénard *et al.* (2018) identified anhydrite and SO_4^{2-}-bearing inclusions in arc peridotite xenoliths, which may suggest that sulfate-bearing fluids penetrate deep into the subarc mantle. However, the input of sulfur into subduction zones is in excess of the volcanic output (Evans, 2012), suggesting that some sulfur may be stored in the mantle wedge.

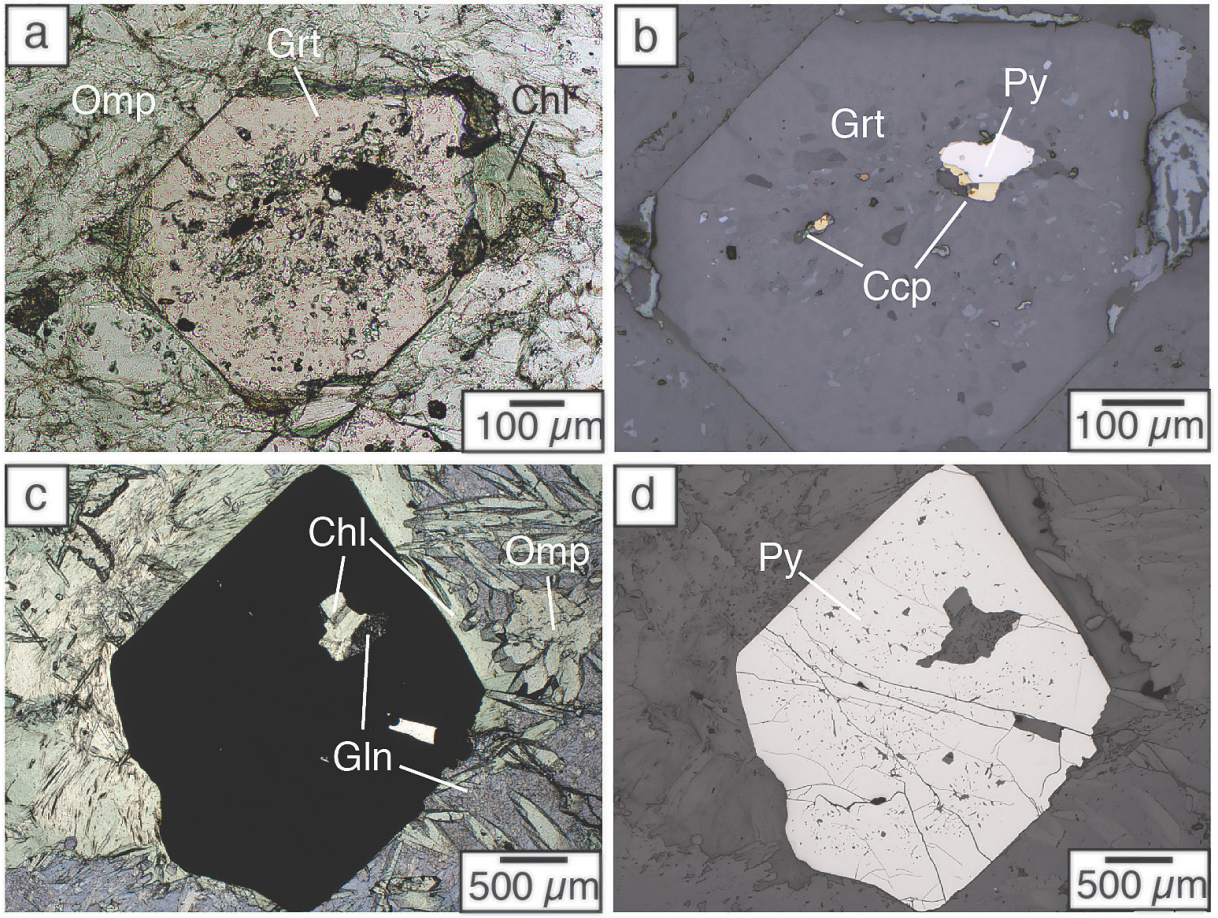

Figure 4 Transmitted **(a,c)** and reflected **(b,d)** light images of sulfides in eclogites. In **(a,b)**, pyrite + chalcopyrite are observed as inclusions in garnet from the Junction School eclogite, Franciscan Complex, California. In **(c,d)**, matrix pyrite is associated with retrograde chlorite + glaucophane in a metasomatised metagabbroic eclogite from Syros, Greece.

Our models allow us to predict on a global scale the influence of sulfur loss on the redox state of volcanic arcs. During "hot" subduction, ~30 % of the total sulfur loss occurs as H_2S and HS^- at shallow depths prior to the sulfide-sulfate transition, followed by a loss of oxidised sulfur at greater depths. Little sulfur is lost prior to the sulfide-sulfate transition in "cold" subduction zones. Therefore, the shallow mantle wedge and forearc magmas may be less oxidised than their arc equivalents. This mechanism is consistent with low $Fe^{3+}/\Sigma Fe$ and sulfur concentrations in Mariana forearc magmas relative to those in the main Mariana arc (Kelley and Cottrell, 2012; Brounce *et al.*, 2014, 2016). The predicted SO_x fluxes are also consistent with the oxidised nature of trench proximal Cu porphyry deposits in the Andes and elsewhere (*e.g.*, Tomkins and Evans, 2015). As a result, arc magmas and subarc mantle in cold subduction zones may be more oxidised relative to hot subduction zones.

Summary

We have demonstrated that sulfur–iron redox reactions in subducting AOC can produce oxidised fluids. Our model predictions are consistent with the petrographic, isotopic, and geochemical record of exhumed high pressure rocks, mantle xenoliths, and arc magmas. Sulfur release is a function of the redox budget of the slab and subduction zone thermal structure, with cold subduction of oxidised crust most efficiently releasing SO_x species. We conclude that sulfur-bearing fluids from AOC may oxidise the arc-mantle system. However, the thermodynamics of sulfur-bearing silicate systems, Fe^{3+} incorporation in silicate minerals, and aqueous sulfur speciation at high pressures remain poorly constrained. It should be a priority for future studies to constrain further our model through the study of natural samples and high pressure experiments.

Acknowledgements

We thank James Connolly for modelling support and Peter van Keken for providing updated *P–T* paths for the Syracuse *et al.* (2010) models. The manuscript benefited from the editorial handling by Helen Williams and from constructive reviews of Maryjo Brounce, Katy Evans, and an anonymous reviewer. JBW acknowledges Fulbright and Chase Distinguished Research fellowships. This work was supported by NSF grant EAR1725301 awarded to AMC.

Editor: Helen Williams

Additional Information

Supplementary Information accompanies this letter at http://www.geochemicalperspectivesletters.org/article2011.

Cite this letter as: Walters, J.B., Cruz-Uribe, A.M., Marschall, H.R. (2020) Sulfur loss from subducted altered oceanic crust and implications for mantle oxidation. *Geochem. Persp. Let.* 13, 36–41.

References

Bénard, A., Klimm, K., Woodland, A.B., Arculus, R.J., Wilke, M., Botcharnikov, R.E., Shimizu, N., Nebel, O., Rivard, C., Ionov, D.A. (2018) Oxidising agents in sub-arc mantle melts link slab devolatilization and arc magmas. *Nature Communications* 9, 1-10.

Birner, S.K., Cottrell, E., Warren, J.M., Kelley, K.A., Davis, F.A. (2018) Peridotites and basalts reveal broad congruence between two independent recorders of mantle fO_2 despite local redox heterogeneity. *Earth and Planetary Science Letters* 494, 172-189.

Blatter, D.L., Carmichael, I.S. (1998) Hornblende peridotite xenoliths from central Mexico reveal the highly oxidized nature of subarc mantle. *Geology* 26, 1035-1038.

Brounce, M.N., Kelley, K.A., Cottrell, E. (2014) Variations in $Fe^{3+}/\Sigma Fe$ of Mariana arc basalts and mantle wedge fO2. *Journal of Petrology* 55, 2514-2536.

Brounce, M., Kelley, K.A., Stern, R., Martinez, F., Cottrell, E. (2016) The Fina Nagu volcanic complex: Unusual submarine arc volcanism in the rapidly deforming southern Mariana margin. *Geochemistry Geophysics Geosystems* 17, 4078-4091.

Brown, J.L., Christy, A.G., Ellis, D.J., Arculus, R.J. (2014) Prograde sulfide metasomatism in blueschist and eclogite, New Caledonia. *Journal of Petrology* 55, 643-670.

Cottrell, E., Kelley, K. (2011) The oxidation state of Fe in MORB glasses and the oxygen fugacity of the upper mantle. *Earth and Planetary Science Letters* 305, 270-282.

Connolly, J.A.D. (2005) Computation of phase equilibria by linear programming: a tool for geodynamic modelling and its application to subduction zone decarbonation. *Earth and Planetary Science Letters* 236, 524-541.

Debret, B., Sverjensky, D.A. (2017) Highly oxidising fluids generated during serpentinite breakdown in subduction zones. *Scientific Reports* 7,10351.

Evans, K.A. (2012) The redox budget of subduction zones. *Earth Science Reviews* 113, 11-32.

Evans, K.A., Tomkins, A.G., Cliff, J., Fiorentini, M.L. (2014) Insights into subduction zone sulfur recycling from isotopic analysis of eclogite-hosted sulfides. *Chemical Geology* 365, 1-19.

Frezzotti, M.L., Ferrando, S. (2015) The chemical behavior of fluids released during deep subduction based on fluid inclusions. *American Mineralogist* 100, 352-377.

Gerrits, A.R., Inglis, E., Dragovic, B., Starr, P.G., Baxter, E.F., Burton, K. (2019) Tracing the source of oxidizing fluids in subduction zones using iron isotopes in garnet. *Nature Geoscience* 12, 1029-1033.

Kelley, K., Cottrell, E. (2009) Water and the oxidation state of subduction zone magmas. *Science* 325, 605-607.

Kelley, K., Cottrell, E., (2012) The influence of magmatic differentiation on the oxidation state of Fe in a basaltic arc magma. *Earth and Planetary Science Letters* 329-330, 109-121.

Lecuyer, C., Ricard, Y. (1999) Long-term fluxes and budget of ferric iron: implications for the redox states of the Earth's mantle and atmosphere. *Earth and Planetary Science Letters* 165, 197-211.

Li, J.L., Schwarzenbach, E.M., John, T., Ague, J.J., Huang, F., Gao, J., Klemd, R., Whitehouse, M.J., Wang, X.S. (2020) Uncovering and quantifying the subduction zone sulfur cycle from the slab perspective. *Nature Communications* 11, 514.

Mackwell, S. (2008) Rheological consequences of redox state. *Reviews in Mineralogy and Geochemistry* 68, 555-569.

McCammon, C.A., Frost, D.J., Smyth, J.R., Lautsen, H.M.S., Kawamoto, T., Ross, N.L., van Aken, P.A. (2004) Oxidation state of iron in hydrous mantle phases: implications for subduction and mantle oxygen fugacity. *Physics of the Earth and Planetary Interiors* 143-144, 157-169.

Mungall, J.E. (2002) Roasting the mantle: Slab melting and the genesis of major Au and Au-rich Cu deposits. *Geology* 30, 915-918.

Spandler, C., Pirard, C. (2013) Element recycling from subducting slabs to arc crust: A review. *Lithos* 170-171, 208-223.

Syracuse, E.M., van Keken, P.E., Abers, G.A. (2010) The global range of subduction zone thermal models. *Physics of the Earth and Planetary Interiors* 183, 73-90.

Tomkins, A.G., Evans, K.A. (2015) Separate zones of sulfate and sulfide release from subducted mafic oceanic crust. *Earth and Planetary Science Letters* 428, 73-83.

Tracy, R.J., Robinson, P. (1988) Silicate-sulfide-oxide-fluid reactions in granulite-grade pelitic rocks, central Massachusetts. *American Journal of Science* 288-A, 45-74.

Walters, J.B., Cruz-Uribe, A.M., Marschall, H.R. (2019) Isotopic compositions of sulfides in exhumed high-pressure terranes: Implications for sulfur cycling in subduction zones. *Geochemistry Geophysics Geosystems* 20, 1-28.

Zack, T., John, T. (2007) An evaluation of reactive fluid flow and trace element mobility in subducting slabs. *Chemical Geology* 239, 199-216.

Geochemical Perspectives Letters

Sulfur loss from subducted altered oceanic crust and implications for mantle oxidation

J.B. Walters, A.M. Cruz-Uribe, H.R. Marschall

Supplementary Information

The Supplementary Information includes:

- S-1 Linking Seafloor Alteration to Pre-subduction Sulfur and Iron Budgets
- S-2 Oxidising the Mantle Wedge – Carbon or Sulfur?
- S-3 Thermodynamic Modelling Methodology
- S-4 Redox Comparison of AOC and High-pressure Equivalents
- Tables S-1 and S-2
- Figures S-1 to S-11
- Supplementary Information References

S-1 Linking Seafloor Alteration to Pre-subduction Sulfur and Iron Budgets

Redox reactions, such as those involving sulfur loss during subduction of AOC, are influenced by the concentration and speciation of redox sensitive elements. The degree of oxidation and sulfur concentration of the oceanic crust are a function of metasomatic reactions prior to subduction. At mid-ocean ridges, the elevated heat flow and structures generated by tectonic rifting promote high-*T* hydrothermal circulation of seawater (Fig. 1). As the crust migrates from the ridge axis, alteration continues at temperatures <150 °C for an average of 65 m.y. (Fisher, 2005). Studies of the oceanic crust show a redistribution and overall loss of sulfur through pervasive oxidation (Alt *et al*., 1989; Alt, 1995; Bach and Edwards, 2003; Alt and Shanks, 2011). Well-studied crustal sections show heterogeneous oxidation and sulfur mobilisation with depth. Here we focus on ODP Hole 504B, which represents the most complete section of oceanic crust drilled to date and is the source of our estimate for the average AOC composition. Additionally, the sulfide-oxide-silicate assemblages have been well documented by Alt *et al.* (1989). During the seafloor alteration process, oxidation begins along fractures to produce oxidation halos. Oxidation decreases with distance from the crack interface. In the upper volcanic zone, igneous chalcopyrite, pyrrhotite, and pentlandite are converted to Fe-oxyhydroxides near the interface and to pyrite ± marcasite with rare chalcopyrite in the less altered interior. Below the volcanic complex, oxide replacements after sulfides are less common, and pyrite dominates the sulfide assemblage. Minor chalcopyrite, bornite (Cu_5FeS_4), sphalerite (ZnS), and millerite (NiS), and rare galena (PbS), carrolite ($Cu(Co,Ni)_2S_4$), and linnaeite (Co_3S_4) have also been observed.

Average MORB contains ~1150 µg/g S, whereas the background alteration of the volcanic section of IODP/ODP holes 504B contains an average of 460 ±340 µg/g S (Hubberten *et al*., 1983; Alt and Emmermann, 1985; Cottrell and Kelley, 2011). In contrast, the sheeted-dyke complex at Hole 504B exhibits bulk S contents of ~720 µg/g (Alt *et al*., 1989; Alt, 1995). Between the sheeted dyke complex and upper volcanic section exists a ~200 m thick sulfur-enriched transition zone that contains sulfide-rich horizons with

up to ~1.5 wt. % S (Alt, 1995). Sulfide enrichment is driven by the mixing between seawater circulating in the volcanic section with high-temperature (250-380 °C) hydrothermal fluids percolating upwards through the sheeted-dyke complex (Fig. 1; Alt *et al.*, 1989). The average S content of Hole 504B calculated here is ~840 μg/g, indicating a net loss during alteration.

Altered oceanic crust contains an average of ~9 wt. % Fe, with an average $Fe^{3+}/\Sigma Fe$ ratio of ~0.28 (Honnorez *et al.*, 1983; Hubberten *et al.*, 1983; Alt and Emmermann, 1985; Emmermann *et al.*, 1985; Alt *et al.*, 1989). In contrast, MORB exhibits an average $Fe^{3+}/\Sigma Fe$ ratio of ~0.14 (Cottrell and Kelley, 2011; Zhang *et al.*, 2018). The upper volcanic section exhibits the greatest oxidation, with an average $Fe^{3+}/\Sigma Fe$ of ~0.35 (Bach and Edwards, 2011). Below the transition zone the average $Fe^{3+}/\Sigma Fe$ decreases to ~0.20.

S-2 Oxidising the Mantle Wedge – Carbon or Sulfur?

Oxidised slab-derived C or S may initiate redox reactions in the overlying mantle wedge depending on the *P–T–X* conditions of the mantle. Unaltered Mid-ocean ridge (MOR) peridotites are less affected by metasomatism and likely exhibit an fO_2 analogous to pre-subduction mantle wedge peridotite. Upper mantle peridotites exposed at mid-ocean ridges (MOR) exhibit a range in ΔQFM from -1.5 to +1 log units with an average of 0.00 ±0.26 2SE (Birner *et al.* 2018). While a 2.5 log unit range is fairly large, approximately 70 % of fO_2 estimates fall at or above QFM. Therefore, ambient redox conditions at or just above QFM are expected for the mantle wedge prior to subduction.

It has long been recognised that the metasomatic addition of CO_2 from the dehydrating slab is unlikely to initiate significant redox reactions in the mantle wedge (*e.g.*, Mungall, 2002). At *P–T* conditions of ≥800 °C and 2.0 GPa, the carbon–carbon oxide (CCO) buffer occurs at oxygen fugacities below QFM (Fig. S-1a). In contrast, graphite (C^0) is stable up to nearly QFM+2 at 500 °C and 2.0 GPa. As a result, C^{4+} in CO_2 may be reduced to graphite and simultaneously oxidise Fe^{2+} at low temperatures immediately after crossing the slab–mantle interface; however, carbon-reducing redox reactions will cease within a few km from the interface as fluids heat above 800 °C due to the higher ambient temperatures of the mantle (Gerya *et al.*, 2002; Syracuse *et al.*, 2010). At ultrahigh-pressure (UHP) conditions the stability field for C^0 is elevated to nearly 1000 °C, which may allow for enhanced oxidation of the subarc mantle near the slab–mantle interface by CO_2 at greater depths (Fig. S-1b). Consistent with these predictions, investigations of suprasubduction mantle from UHP continental subduction terranes reveal mixed $C–H_2O–CO_2$ fluids in metasomatised ultramafic rocks at oxygen fugacities below QFM, whereas $CO_2–H_2O$ fluids occur at more oxidising conditions (Malaspina *et al*. 2009, 2010, 2012). Core-to-rim increases in garnet Fe^{3+} contents in these peridotites are consistent with C-reducing Fe-oxidising reactions (Tumiati and Malaspina, 2019). We suggest diverging relationships between slab-derived carbon and the oxidation of the mantle wedge for oceanic and continental subduction, respectively. For subducting oceanic lithosphere, the majority of H_2O is lost before the slab reaches subarc depths (van Keken *et al*., 2011), whereas significant H_2O subduction beyond subarc depths may occur during the subduction of continental crust (Hacker, 2008). Therefore, limited exchange of mixed $H_2O–CO_2$ fluids is expected at depths where the CCO buffer is sufficiently elevated relative to QFM. At the other extreme, carbonate reduction has been observed at low *P–T* conditions (less than 1.5 GPa and 450 °C; Galvez *et al*., 2013; Vitale Brovarone *et al*., 2017). Therefore, carbonate reduction to graphite or CH_4 may be an important process for oxidising the cold forearc mantle, where the CCO buffer is elevated with respect to QFM. These data suggest that while carbon oxidising reactions may occur in suprasubduction mantle at shallow depths or deep within continental subduction zones, CO_2 likely plays a minor role in initiating redox reactions in the subarc mantle during the subduction of oceanic lithosphere.

With the exception of low temperature–ultrahigh pressure conditions, SO_4^{2-} is stable at oxygen fugacities significantly higher than the CCO buffer. For example, the fO_2 of the reaction $FeS + CaFeSi_2O_6 + 2O_2 = CaSO_4 + 2FeSiO_3$ occurs at 1 to 2.5 log units above the CCO buffer from 500 to 1200 °C at 2.0 GPa (Fig. S-1a). Therefore, sulfur reducing–iron oxidising reactions may operate in the subarc mantle at fO_2 conditions beyond those at which CO_2 may oxidise iron. Sulfate addition will oxidise iron in the mantle wedge until the SSO buffer is reached (Mungall, 2002), above which sulfate is stable and further addition will not initiate redox reactions. In the aforementioned scenario, progressive slab-derived sulfate-bearing fluids overcome the redox buffering capacity of the solid silicate and oxide phases in mantle peridotite. Arc xenoliths commonly record oxygen fugacities of QFM to QFM+2 (*e.g.*, Brandon and Draper, 1996; Blatter and Carmichael, 1998; Peslier *et al*., 2002; Parkinson *et al*., 2003), a range that is consistent with the maximum limit for mantle oxidation by sulfate reduction.

S-3 Thermodynamic Modelling Methodology

Model design

Thermodynamic models were generated following the methods of Connolly and Galvez (2018) with Perple_X (Connolly, 2005) version 6.8.4 using the HP62 and DEW17 thermodynamic databases (Holland and Powell, 2011; Sverjensky *et al.*, 2014). The bulk composition for the average AOC models was calculated using an average crustal section for ODP Hole 504B (Honnorez *et al.*, 1983;

Hubberten *et al.*, 1983; Alt and Emmermann, 1985; Emmermann, 1985; Alt *et al.*, 1989) and the mass balance constraints of Alt (1995). An average composition for Hole 504B was selected as it represents the most complete section of oceanic crust drilled to date, thereby capturing the variability of sulfur content and oxidation with depth. The bulk composition for the average MORB models was calculated using the data of Cottrell and Kelley (2011). Water concentrations were estimated for both AOC and MORB bulk compositions by calculating H_2O saturation at the first *P-T* step on the Honshu and Cascadia paths (see below). The bulk composition of the AOC path was used for closed system calculations (*e.g.*, Fig. 2). Potassium was excluded from the bulk composition due to the stabilisation of biotite to unreasonably high *P–T* conditions. Titanium was found to destabilise calculations and was also excluded. While Cl is likely to enhance sulfate solubility (Newton and Manning, 2005), Cl is not included as a potential component in solution models for solid phases and inclusion of Cl would destabilise fluid fractionation (open system) models. The bulk compositions used for AOC and MORB are shown in Table S-1. The following solution models were used in all calculations: Gt (WPH), Omph(GHP), cAmph(G), Chl(W), Ep(HP11), Pl(I1,HP), Po(HP), and COH-Fluid+ (Green *et al.*, 2007; White *et al.*, 2007; Evans *et al.*, 2010; White *et al.*, 2014; Green *et al.*, 2016; Connolly and Galvez, 2018). Talc, lawsonite, quartz, anhydrite, and pyrite were considered to pure phases. Hematite and magnetite were also considered as pure phases and were found to be unstable under the *P–T* conditions examined here. Furthermore, models for spinel solid solution were tested for AOC and MORB models over the *P–T* range of interest; however, spinel was found to be unstable and was not included in further calculations. Fluid fractionation (open system) models were calculated along slab-top geothermal gradients for the D80 models of Syracuse *et al.* (2010). Solute-bearing fluids were extracted at 1 °C intervals from 400 °C until H_2O is fully extracted from the bulk composition along the Honshu and Cascadia *P–T* paths for endmember cold and hot subduction zone geotherms, respectively. A slab-top geothermal gradient is a reasonable choice for modelling dehydration processes for the mafic altered oceanic crust, which typically comprises the uppermost level of subducting slabs. Choice of gradient representing the interior of the slab, such as one along the Mohorovičić discontinuity, would shift the *P-T* path down temperature and up pressure. Therefore, a path along the Mohorovičić discontinuity, is likely to produce elevated SO_x fluxes from the slab given the predicted *P-T* dependency of sulfur oxidation (see main text).

In our study sulfur speciation and fO_2 may vary as a function of equilibrium thermodynamics for a given bulk-rock composition and protolith $Fe^{3+}/\Sigma Fe$ ratio. In Perple_X, the bulk composition is oxidised by providing excess O_2, which may then be assigned to a mineral, fluid, or solute species to oxidise iron or sulfur. Therefore, we add excess O_2 to our bulk compositions consistent with the $Fe^{3+}/\Sigma Fe$ ratios of 0.28 and 0.14 calculated for AOC and MORB, respectively (Honnorez *et al.*, 1983; Hubberten *et al.*, 1983; Alt and Emmermann, 1985; Emmermann *et al.*, 1985; Alt *et al.*, 1989; Cottrell and Kelley, 2011; Zhang *et al.*, 2018). In contrast to the value used here, Berry *et al.* (2018) estimated an average MORB $Fe^{3+}/\Sigma Fe$ ratio of 0.10. The 4 % difference in $Fe^{3+}/\Sigma Fe$ ratios between 0.14 and 0.10 is anticipated to produce slightly more reducing conditions for the MORB models, further accentuating the differences in fluid speciation and sulfur loss we observe between AOC and MORB models. The assignment of the added O_2 is dictated by minimising Gibbs free energy at a given point in *P–T–X* space. This technique has the advantage of allowing the system to evolve naturally, rather than applying an external O_2 buffer to the system.

Guide to model figures and plots

In the main text, a simplified thermodynamic *P–T* assemblage diagram (Fig. 2) and cumulative sulfur and water loss models (Fig. 3) for AOC are presented. The supplement includes complementary figures for MORB, as well as additional *P–T* assemblage, fluid chemistry, $Fe^{3+}/\Sigma Fe$, and modal abundance plots. Figures in the supplement are organised into AOC (Figs. S-2 to S-5) and MORB (Fig. S-6 to S-11). Simplified (Figs. 2 & S-6) and labelled (Figs. S-2 & S-5) *P–T* phase diagrams are shown. All other figures contain data for both the Honshu and Cascadia *P–T* paths. Sulfur and fluid loss models are shown in Figures 3 (AOC) and S-8 (MORB). Fluid chemistry models, highlighting changes in sulfur molality, cation molality, and pH, are included for fluid fractionation of AOC (Fig. S-3) and MORB (Fig. S-9). Figures show the modal evolution of the solid sulfur phases and $Fe^{3+}/\Sigma Fe$ ratio to subduction dehydration and sulfur-iron redox reactions. Finally, the evolution of the silicate mineralogy as a function of *P–T* and dehydration are shown for AOC (Fig. S-5) and MORB (S-11).

Comparison with previous modelling studies

Previous models of sulfur redox in high-pressures rocks hinge on assumptions which restrict the behaviour of the system. For example, Tomkins and Evans (2015) calculated sulfate loss from AOC during dehydration. Sulfur is not explicitly included in their thermodynamic models; instead, the amount of sulfate lost to anhydrite dissolution is calculated separately at each step along the modelled dehydration paths. The addition of sulfur to the Holland and Powell (2011) database and the development of a solid-solution model for pyrrhotite (Evans *et al.*, 2010) allowed for the direct incorporation of sulfur into thermodynamic simulations in our models. For example, Evans and Powell (2015) considered Fe-sulfides and sulfur-bearing fluids in open and closed system during subduction of hydrated lithospheric mantle. However, Evans and Powell (2015) restricted the fluid composition to incorporate H_2S as the only sulfur volatile species. In contrast, we utilise the Deep Earth Water (DEW) model of Sverjensky *et al.* (2014) to consider a large range of fluid mobile sulfur solute and solvent species.

While the previous studies of Debret and Sverjensky (2017) and Connolly and Galvez (2018) also apply the DEW model, both studies make simplifications that distinguish them from the treatment presented here. Debret and Sverjensky (2017) applied the DEW model to examine the redox state of fluids generated during serpentinite dehydration. In their study, oxidised sulfur species were predicted to dissolve in an aqueous fluid produced by antigorite breakdown between 630 and 660 °C at a constant pressure of 2.0 GPa. However, the model of Debret and Sverjensky (2017) did not account for mineral solid solution and only a small 30 °C portion of the slab *P–T* path was explored. In contrast, Connolly and Galvez (2018) combined the DEW model with the Perple_X thermodynamic modelling software, allowing for a thorough treatment of mineral solid solution and fluid speciation along a complete subduction geothermal gradient. A sedimentary bulk composition was used, and ferric iron was not considered. The simplifications of both studies are avoided here. Like Connolly and Galvez (2018), we consider the influence of mineral solid solution on sulfur speciation in the fluid; however, we also apply realistic $Fe^{3+}/\Sigma Fe$ ratios for subducted AOC and MORB. The distinction is critical: Without including ferric iron the proposed sulfur oxidising–iron reducing reactions proposed in this study would not be possible. Additionally, these studies examine ultramafic and sedimentary bulk compositions, which are not considered in our study.

Potential caveats

Perple_X may only model redox reactions involving an exchange of O_2 between the reactant being reduced and the product being oxidised. For example, O_2 is transferred from Fe_2O_3 to $CaSO_4$ during the oxidation of sulfur from S^- in FeS_2 to $S6^+$ in $CaSO_4$. Therefore, changes in $Fe^{3+}/\Sigma Fe$ in Perple_X may be calculated through O_2 mass balance. In the case of the oxidation of S^{2-} in pyrrhotite to S^{1-} in pyrite, the oxidised phase on the right side of the redox reaction does not receive O_2 (there is no O_2 in FeS_2); therefore, no change in $Fe^{3+}/\Sigma Fe$ is observed (Fig. S-3). Only 1 mol of Fe^{3+} may be reduced for every 1 mol of S^{2-} oxidised to S^{1-}. We calculate a 7 % decrease in the bulk O_2 content associated with pyrrhotite to pyrite transition (0.27 to 0.25 wt. % O_2). We found that running our calculation at 0.25 wt. % O_2 instead of 0.27 wt. % O_2 does not significantly influence our results.

S-4 Redox Comparison of AOC and High-pressure Equivalents

Here we provide a comparison of the oxidation state of iron against estimated $Fe^{3+}/\Sigma Fe$ ratios for typical blueschist- and eclogite-facies assemblages. We have compiled average, minimum, and maximum $Fe^{3+}/\Sigma Fe$ ratios and FeO_T (wt. %) for omphacite, garnet, glaucophane, and chlorite (see Table S-2). Data are from Coleman *et al.* (1965), Ernst *et al.* (1970), Ernst and Wai (1970), Enders et al. (2000), Schmid *et al*. (2003), Proyer *et al.* (2004), Li *et al*. (2005), and Masci *et al.* (2019). Ferric and ferrous iron partition into different phases; therefore, bulk rock $Fe^{3+}/\Sigma Fe$ ratios are a more effective means of examining redox reactions. We construct probable bulk rock $Fe^{3+}/\Sigma Fe$ ratios for blueschist and eclogite using mineral $Fe^{3+}/\Sigma Fe$ and Fe contents for a range of mineral abundances. This method is preferred to bulk rock composition measurements, which artificially mix mineral domains that represent different phases of subduction metamorphism. There is significant scatter in reported $Fe^{3+}/\Sigma Fe$ ratios (*e.g.*, omphacite $Fe^{3+}/\Sigma Fe$ ratios range from 0.2 to 0.8), which likely reflect variations in bulk rock $Fe^{3+}/\Sigma Fe$ as well as differences in *P-T*. Therefore, it is not entirely appropriate to mix $Fe^{3+}/\Sigma Fe$ ratios analyses from different samples. However, these data provide the best estimates for prograde changes in $Fe^{3+}/\Sigma Fe$ in the absence of studies where $Fe^{3+}/\Sigma Fe$ data for a single suite of rocks across the blueschist- to eclogite-facies transition.

Fully dehydrated eclogites are dominated by garnet + omphacite, with minor kyanite, rutile, and quartz. Omphacite may contain up to ~0.64 $Fe^{3+}/\Sigma Fe$ in eclogite, whereas garnet exhibits $Fe^{3+}/\Sigma Fe$ ratios <0.1. While omphacite may partition Fe^{3+} over garnet, garnets contain on average 4 times greater FeO_T (wt. %). Therefore, the $Fe^{3+}/\Sigma Fe$ budget of eclogites is largely a function of garnet abundance. For average garnet and omphacite compositions, an eclogite with equal volume proportions of omphacite and garnet is estimated to have an $Fe^{3+}/\Sigma Fe$ ratio of 0.1. In contrast, the $Fe^{3+}/\Sigma Fe$ ratio increases to 0.25 for an eclogite with a 9:1 ratio of omphacite to garnet. A 1:1 ratio of omphacite to garnet using a more extreme omphacite composition ($Fe^{3+}/\Sigma Fe$ = 0.65, FeO_T = 0.32 apfu) results in bulk $Fe^{3+}/\Sigma Fe$ of ~0.2. These calculations suggest that, with the exception of assemblages dominated by omphacite, eclogites likely exhibit lower $Fe^{3+}/\Sigma Fe$ ratios compared to average AOC.

Blueschists seem to exhibit more oxidised assemblages. Most Fe-bearing silicate minerals in blueschists, such as glaucophane, chlorite, and epidote, may contain appreciable ferric iron. The $Fe^{3+}/\Sigma Fe$ ratio reported by Masci *et al.* (2019) appears high; however, the high Fe^{3+} contents do not appear to be a result of beam oxidation or orientation dependence of the near-edge spectra. A lawsonite blueschist with 70 vol % glaucophane, 10 vol % chlorite, and 20 vol % lawsonite is estimated to have a bulk $Fe^{3+}/\Sigma Fe$ ratio of 0.32. Therefore, blueschists exhibit similar bulk $Fe^{3+}/\Sigma Fe$ ratios to AOC, whereas eclogites are reduced.

Supplementary Tables

Table S-1 Bulk rock compositions used for thermodynamic models, expressed as wt. % oxides.

	Average AOC		Average MORB	
	Honshu P-T path	Cascadia P-T path	Honshu P-T path	Cascadia P-T path
SiO_2	47.559	49.084	48.669	51.540
Al_2O_3	14.923	15.402	15.184	16.080
FeO	8.749	9.034	9.122	9.660
MgO	8.288	8.559	7.639	8.090
CaO	12.132	12.522	10.954	11.600
Na_2O	1.964	2.029	2.606	2.760
S_2	0.085	0.084	0.113	0.120
O_2	0.273	0.280	0.142	0.150
H_2O	6.028	3.008	5.570	3.029

Table S-2 Average compositions (wt. %) and $Fe^{3+}/\sum Fe$ ratios of common HP minerals.

	Omphacite (n=34)		Garnet (n=27)		Glaucophane (n=14)		Chlorite (n=5)	
	Mean	2SE	Mean	2SE	Mean	2SE	Mean	2SE
SiO_2	55.23	0.67	38.62	0.37	54.50	1.17	25.95	2.11
TiO_2	0.18	0.17	0.98	0.10	0.30	0.13	-	-
Al_2O_3	9.73	0.74	20.68	1.60	7.57	1.88	20.10	1.95
Cr_2O_3	0.06	0.01	-	-	-	-	-	-
Fe_2O_3	2.04	0.81	1.45	0.18	6.94	2.80	8.35	3.09
FeO	2.67	0.41	22.01	1.49	12.49	2.48	17.48	7.37
MnO	0.04	0.02	0.78	0.32	0.72	0.80	0.28	0.10
MgO	9.51	0.64	6.26	1.25	7.39	2.12	15.82	4.61
CaO	14.05	1.03	9.20	0.95	1.56	0.91	-	-
Na_2O	6.01	0.61	-	-	6.23	0.44	-	-
K_2O	0.03	0.02	-	-	0.13	0.06	-	-
Total	99.52	0.24	99.81	0.14	97.79	0.32	87.99	0.37
Si	1.969	0.012	2.981	0.011	7.819	0.089	2.680	0.137
Ti	0.005	0.005	0.014	0.006	0.032	0.013	0.000	0.000
Al	0.408	0.030	1.947	0.019	1.265	0.308	4.918	0.636
Cr	0.002	0.001	-	-	-	-	0.000	0.000
Fe^{3+}	0.068	0.020	0.085	0.010	0.777	0.329	0.645	0.232
Fe^{2+}	0.081	0.012	1.433	0.114	1.545	0.336	1.533	0.695
Mn	0.001	0.001	0.060	0.028	0.097	0.103	0.024	0.008
Mg	0.509	0.035	0.720	0.137	1.556	0.438	2.419	0.373
Ca	0.539	0.042	0.762	0.080	0.238	0.140	-	-
Na	0.413	0.041	-	-	-	-	-	-
K	0.001	0.001	-	-	-	-	-	-
Total	3.995	0.011	8.005	0.027	15.080	0.127	12.218	0.373
$\sum Fe$	0.15	0.02	1.52	0.12	2.32	0.64	2.18	0.52
$Fe^{3+}/\sum Fe$	0.43	0.05	0.06	0.01	0.31	0.07	0.33	0.15

Supplementary Figures

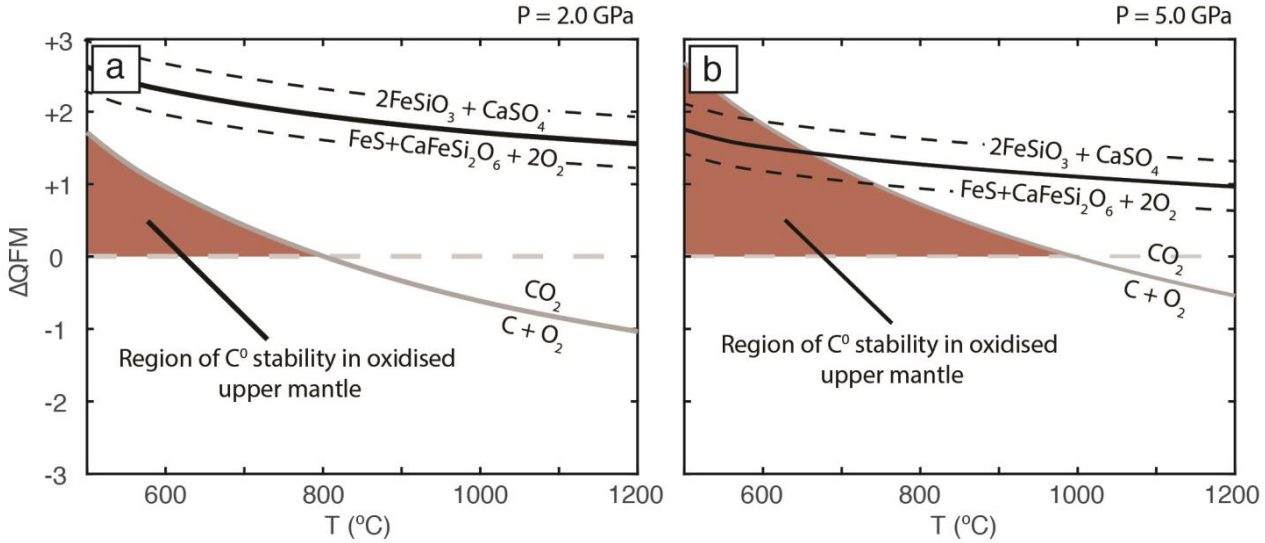

Figure S-1 Diagrams showing the $C + O_2 = CO_2$ (CCO) and $FeS + CaFeSi_2O_6 + 2O_2 = 2FeSiO_3 + CaSO_4$ (SSO) buffer reactions as a function of temperature and fO_2 at (a) 2.0 GPa and (b) 5.0 GPa. Upper and lower bounds (dashed lines) show the position of the SSO buffer at $a CaFeSi_2O_6$=0.2 and $a FeSiO_3$=0.2, respectively. Oxygen fugacity is reported relative to QFM. Calculations were performed using the thermodynamic database and methodology of Holland and Powell (2011). The region in which C^0 may be stable above the QFM buffer is highlighted in red.

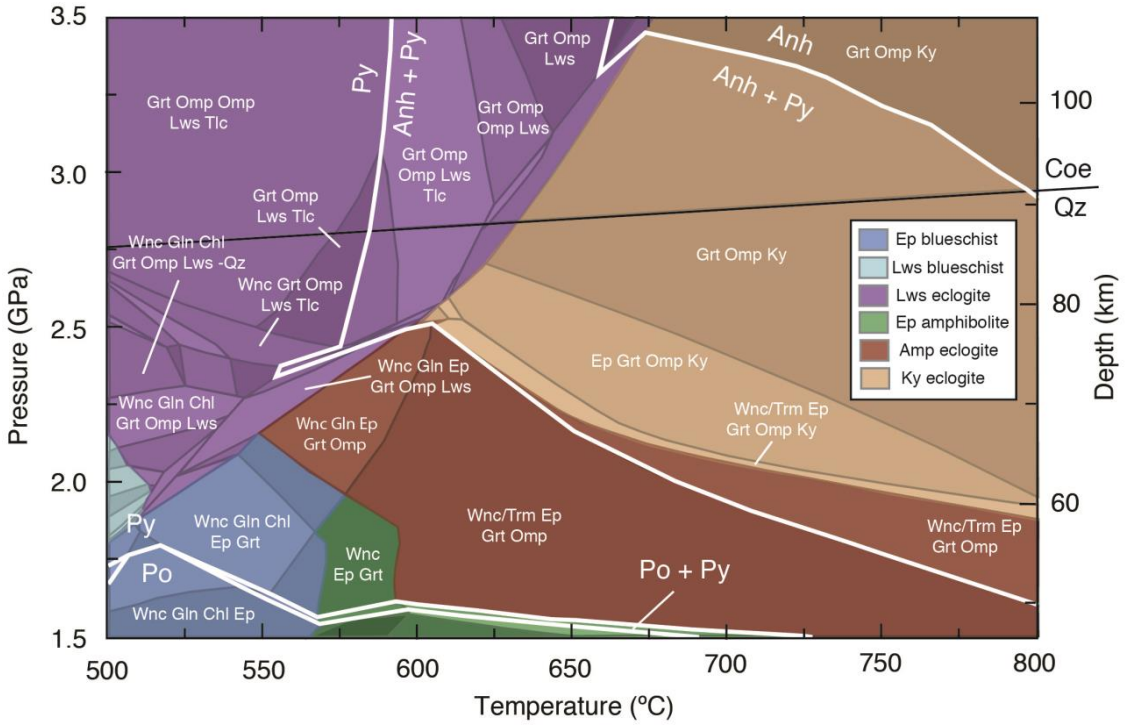

Figure S-2 Phase equilibrium modelling results utilising an average AOC composition (Table S-1). Major mineral assemblages are labelled for large fields. Mineral abbreviations follow Whitney and Evans (2010). Fluid and quartz/coesite are present in all fields. The stability fields of various rock types are shaded (see key), the quartz–coesite transition, and the stable solid sulfur phases are also highlighted.

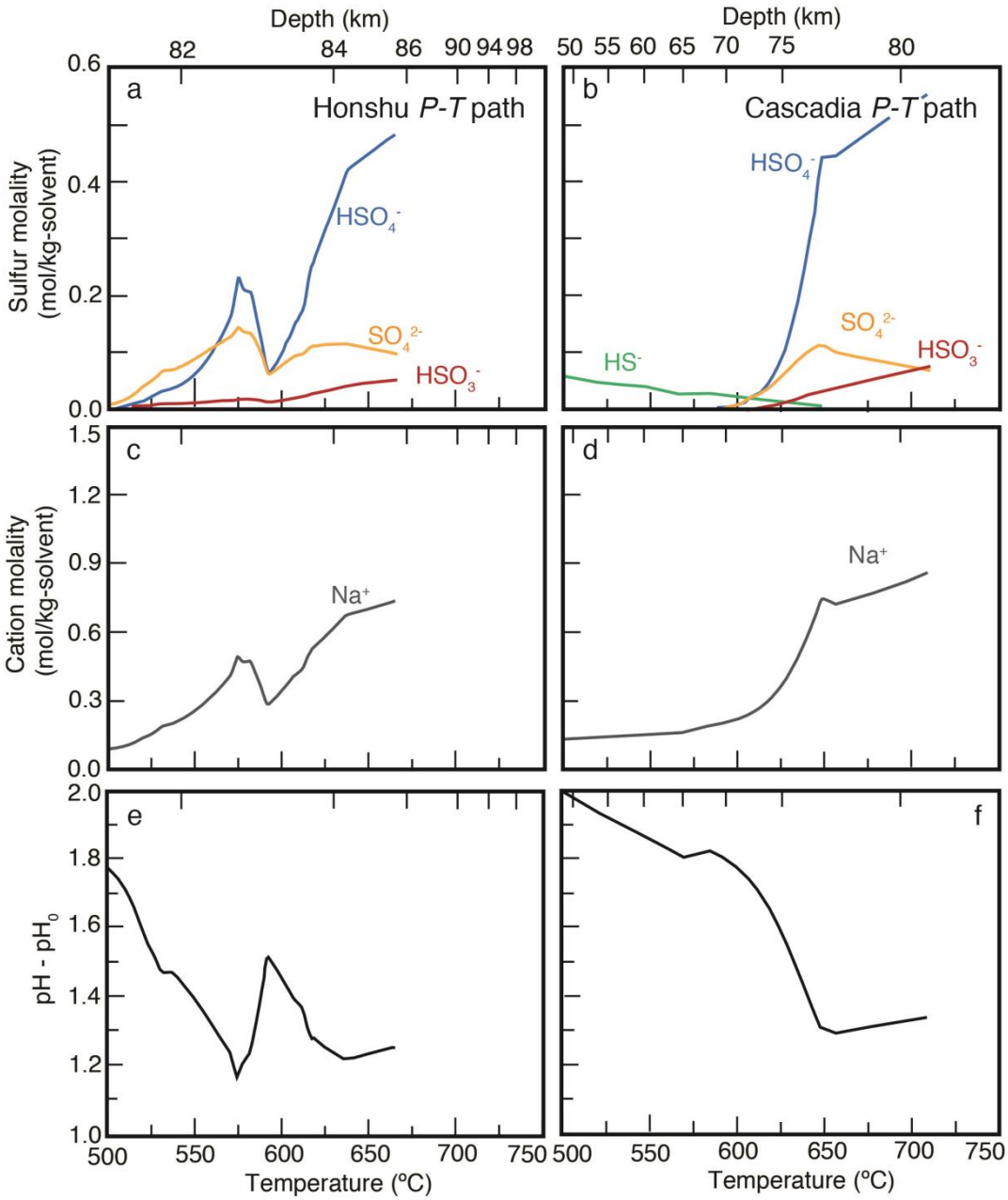

Figure S-3 Plots of sulfur molality **(a-b)**, cation molality **(c-d)**, and pH-pH_0 **(e-f)** against *T* and depth for fluids fractionated (open system) along the Honshu and Cascadia *P-T* paths for an average AOC composition. The sulfur species HSO_4^-, SO_4^{2}, and HSO_3^- are dominant along the Honshu path, with other sulfur species occurring at molalities <<0.1 mol/kg. In contrast, HS^- is present in appreciable concentrations prior to the sulfide–sulfate transition along the Cascadia path. In both cases, the molality of sulfur anions is balanced by the presence of Na^+ cations. Plots of pH-pH_0, which correct for the *P–T* dependence of neutral pH, show decreasing pH associated with the formation of HSO_4^- and HSO_3^- which are conjugate bases of sulfuric and sulfurous acids, respectively.

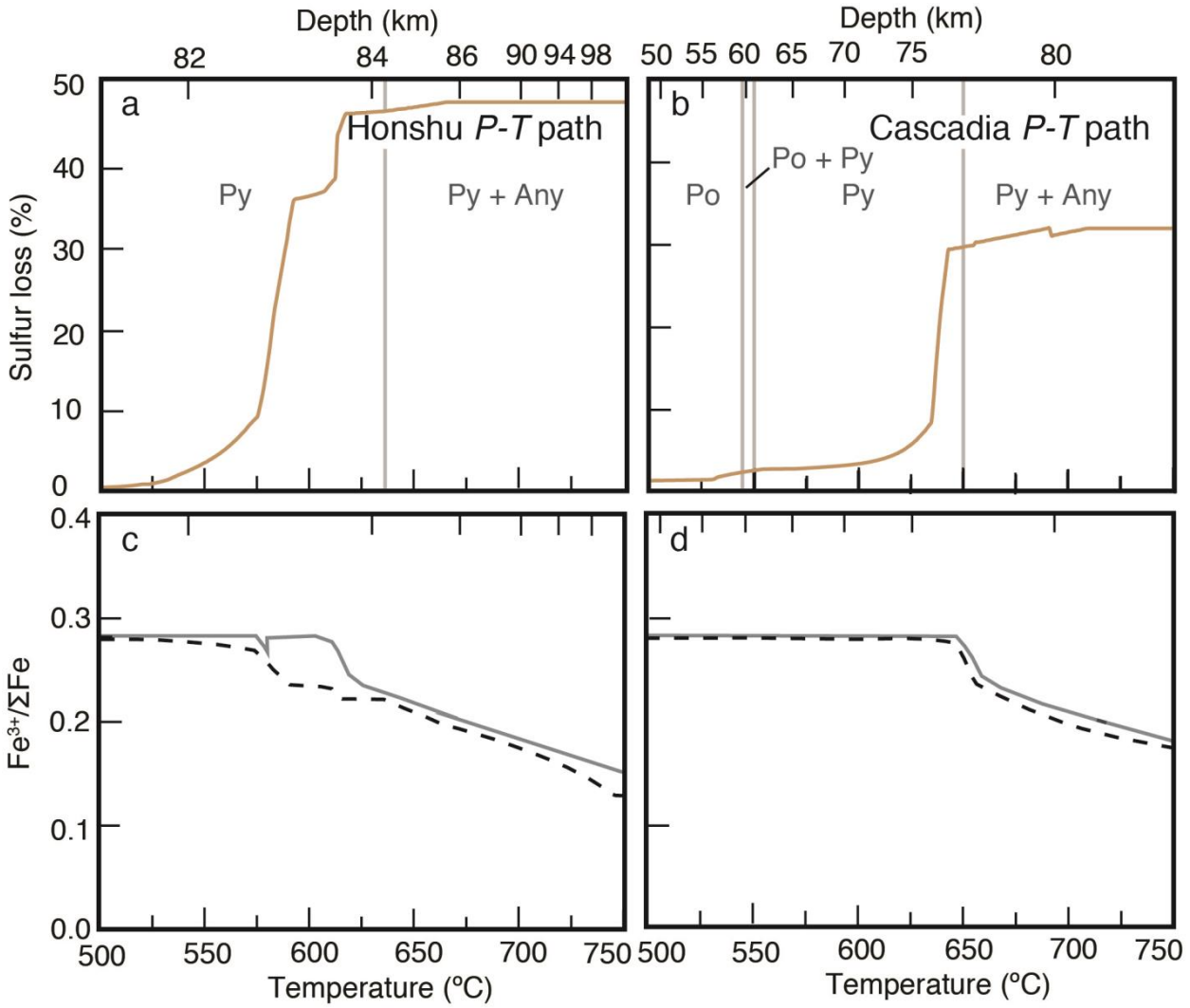

Figure S-4 Plots of percent sulfur loss **(**sulfur loss/initial sulfur concentration, **a-b)** and bulk rock $Fe^{3+}/\Sigma Fe$ **(c-d)** against temperature and depth along the Honshu and Cascadia *P–T* paths for an average AOC composition. Bulk rock $Fe^{3+}/\Sigma Fe$ ratio is plotted for both closed (solid grey) and open (dashed black) systems. Sulfide/sulfate assemblages are also shown in grey. The bulk rock $Fe^{3+}/\Sigma Fe$ ratio decreases with increasing sulfur loss as a function of increasing temperature and depth. Deviations between the closed and open system $Fe^{3+}/\Sigma Fe$ ratios are a result of the loss of SO_x species.

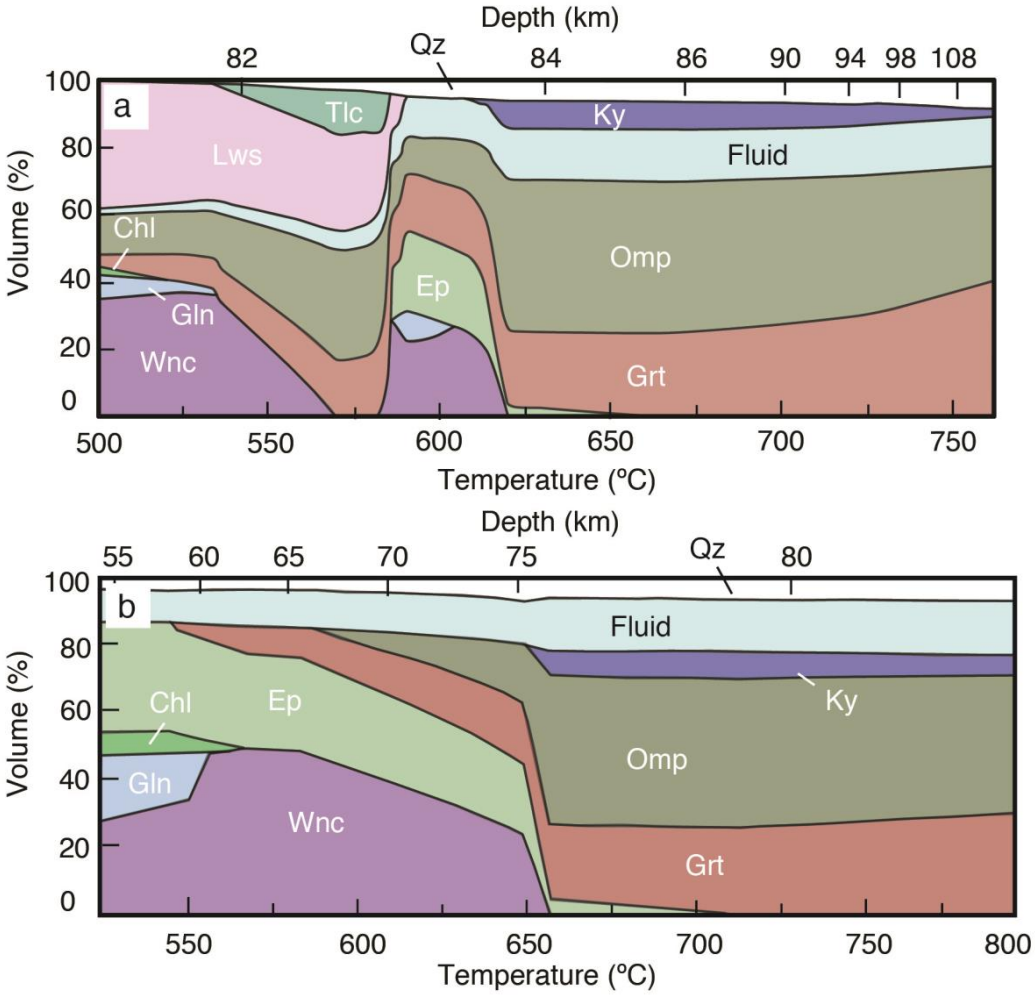

Figure S-5 Plots of major mineral abundances *vs*. temperature and depth for **(a)** Honshu and **(b)** Cascadia *P*–*T* paths for the closed system AOC model. Mineral abbreviations are after Whitney and Evans (2010).

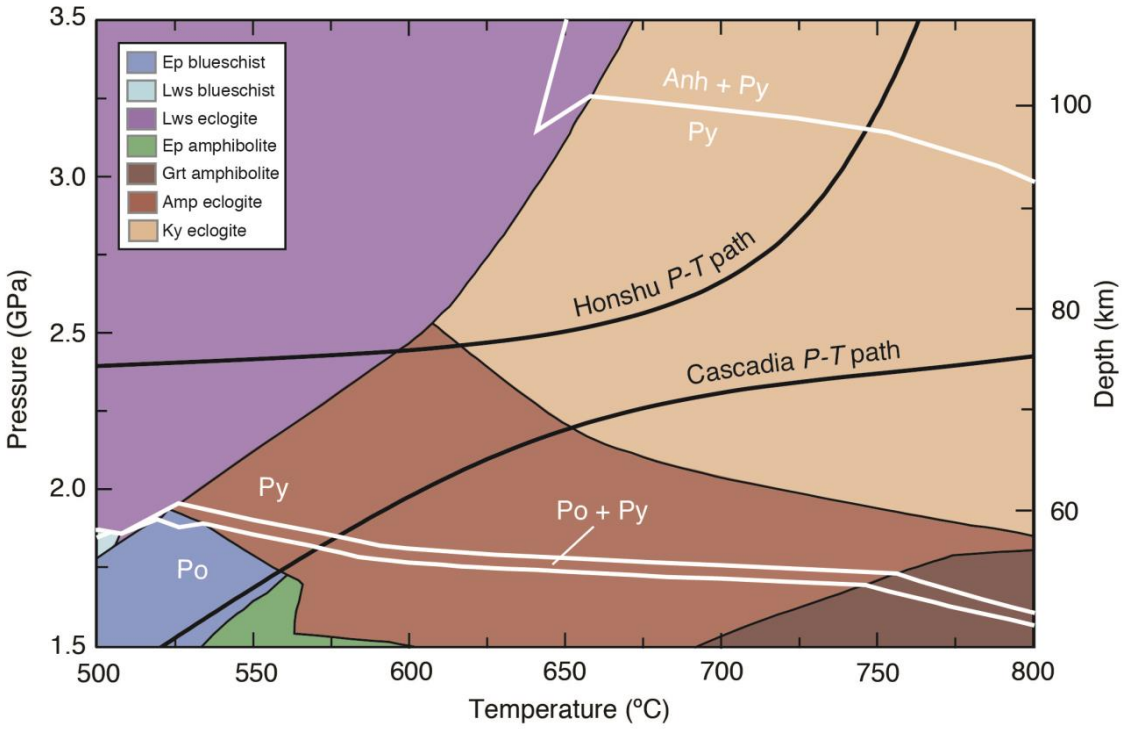

Figure S-6 Phase equilibrium modelling results utilising an average MORB composition (Table S-1) for comparison with Figure 2. The stability fields of various rock types are shaded (see key) and the stable solid sulfur phases are also highlighted. Pyrrhotite stability is shifted up pressure by ~0.4 GPa, whereas the anhydrite in reaction is shifted up *P* by ~1 GPa, relative to AOC. As a result, the fO_2 buffering assemblage of anhydrite + pyrite will not influence fluid compositions prior to complete dehydration (see Fig. S-7).

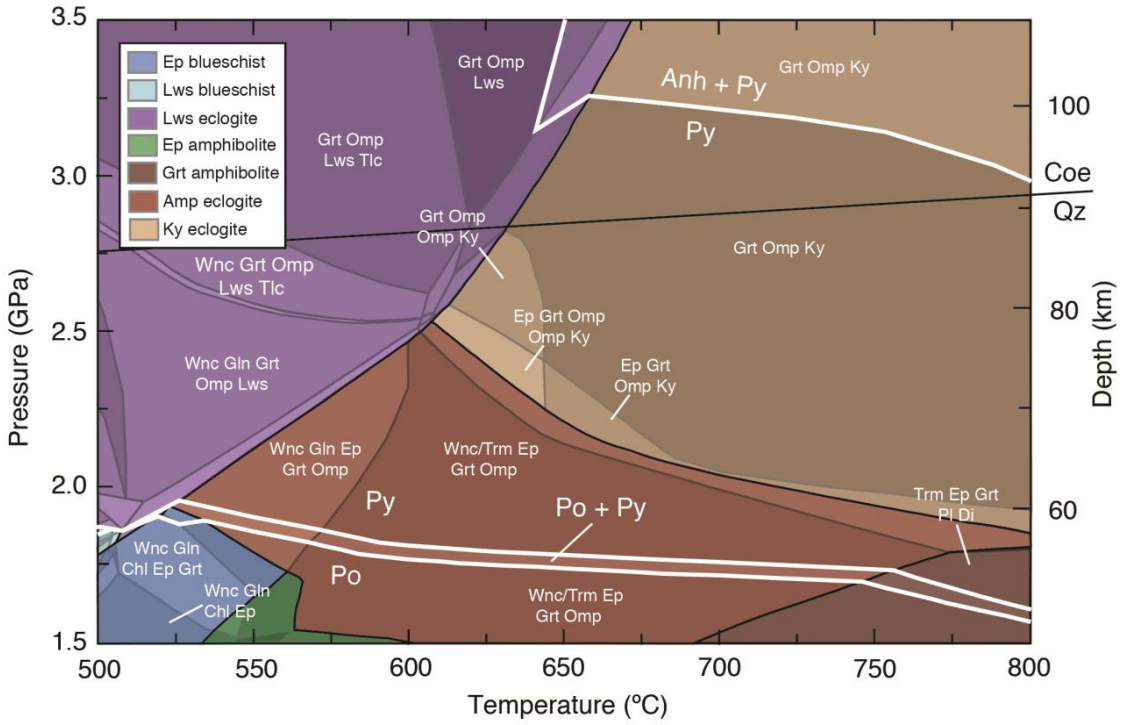

Figure S-7 Phase equilibrium modelling results utilising an average MORB composition (Table S-1) for comparison with Figure S-1. Major mineral assemblages are labelled for large fields. Fluid and quartz/coesite are present in all fields. The stability fields of various rock types are shaded (see key), the quartz-coesite transition, and the stable solid sulfur phases are also highlighted. In comparison with the diagram for AOC (Fig. S-1), chlorite is unstable at higher *P* and the amphibole eclogite assemblage is stabilised to lower *P*. A field representing a garnet amphibolite assemblage is also present at high-*T* and low-*P* but was not present in the AOC composition. Additionally, lawsonite blueschist field is suppressed to lower *P*–*T*.

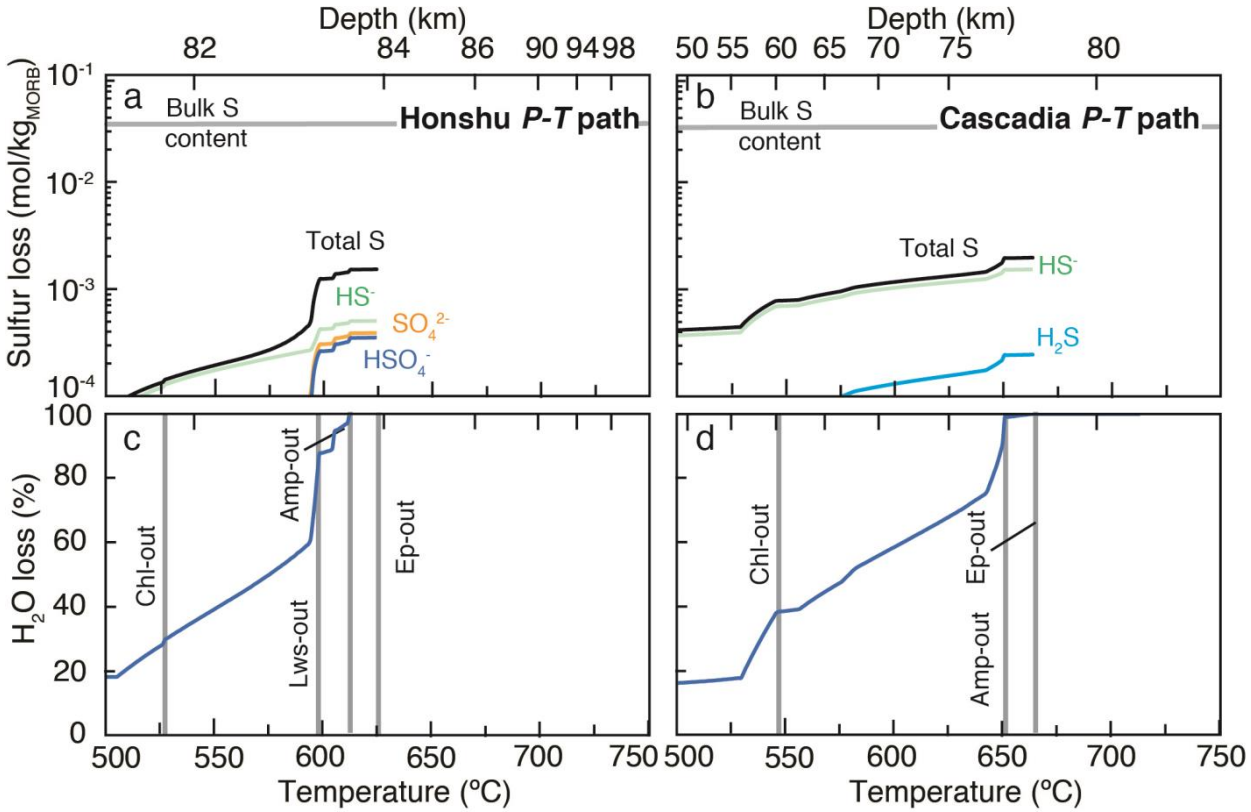

Figure S-8 Cumulative sulfur **(a-b)** and fluid **(c-d)** loss diagrams for fluids fractionated along the Honshu and Cascadia *P-T* paths for a MORB composition. Both temperature and the corresponding slab-top depth are plotted on the x-axis. Key dehydration reactions along each *P-T* path are also shown for reference. Along the Honshu and Cascadia paths, the amount of sulfur lost is nearly an order of magnitude lower for MORB compared to AOC.

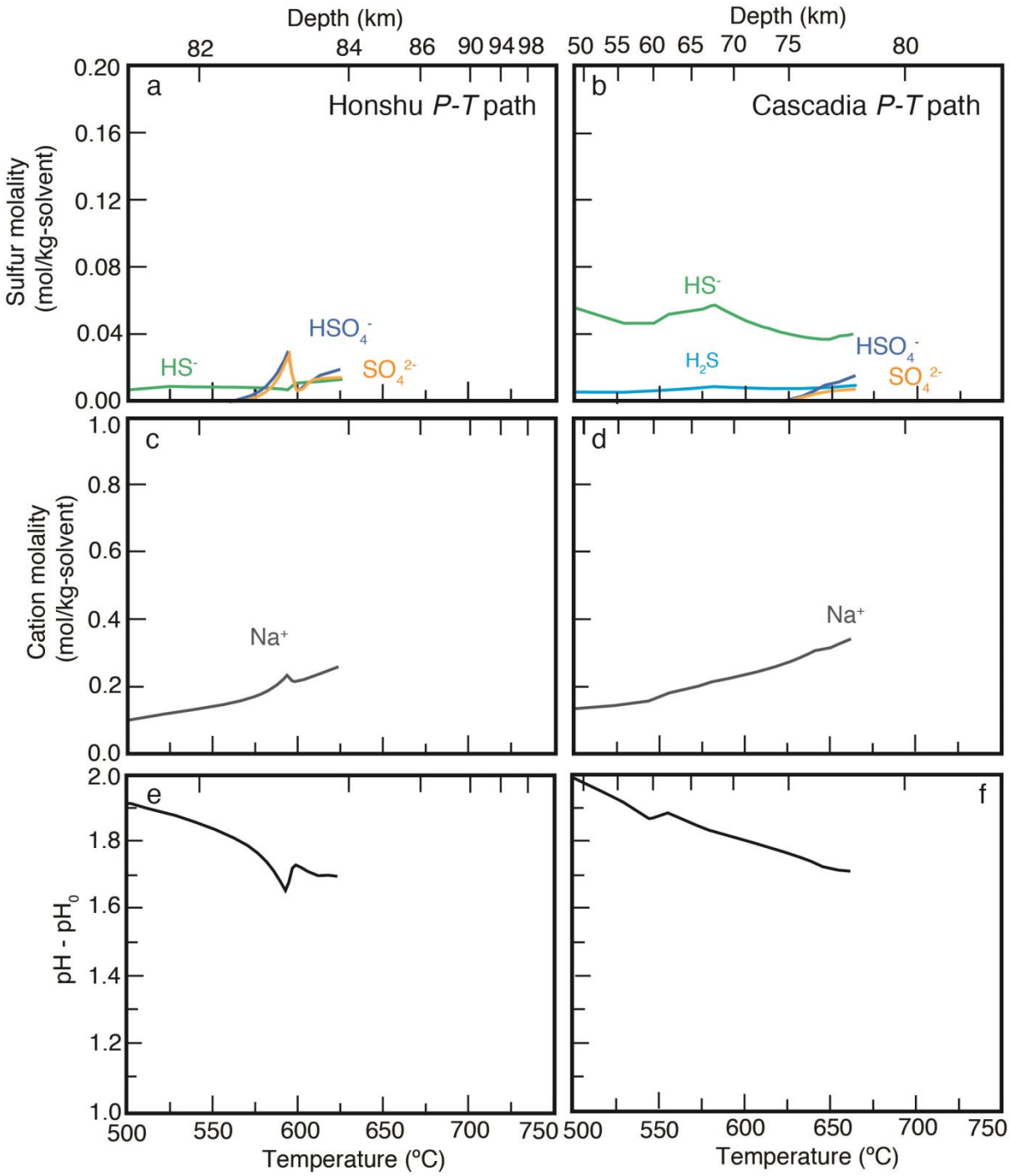

Figure S-9 Plots of sulfur molality **(a-b)**, cation molality **(c-d)**, and pH-pH_0 **(e-f)** against *T* and depth for fluids fractionated (open system) along the Honshu and Cascadia *P–T* paths for an average MORB composition. Sulfur molalities are an order of magnitude lower for MORB compared to AOC (Fig. S-2). Additionally, Na^+ molality and pH mostly do not reflect the behaviour of sulfur species in the fluid in the Cascadia path, suggesting other anion species are responsible for the observed trends.

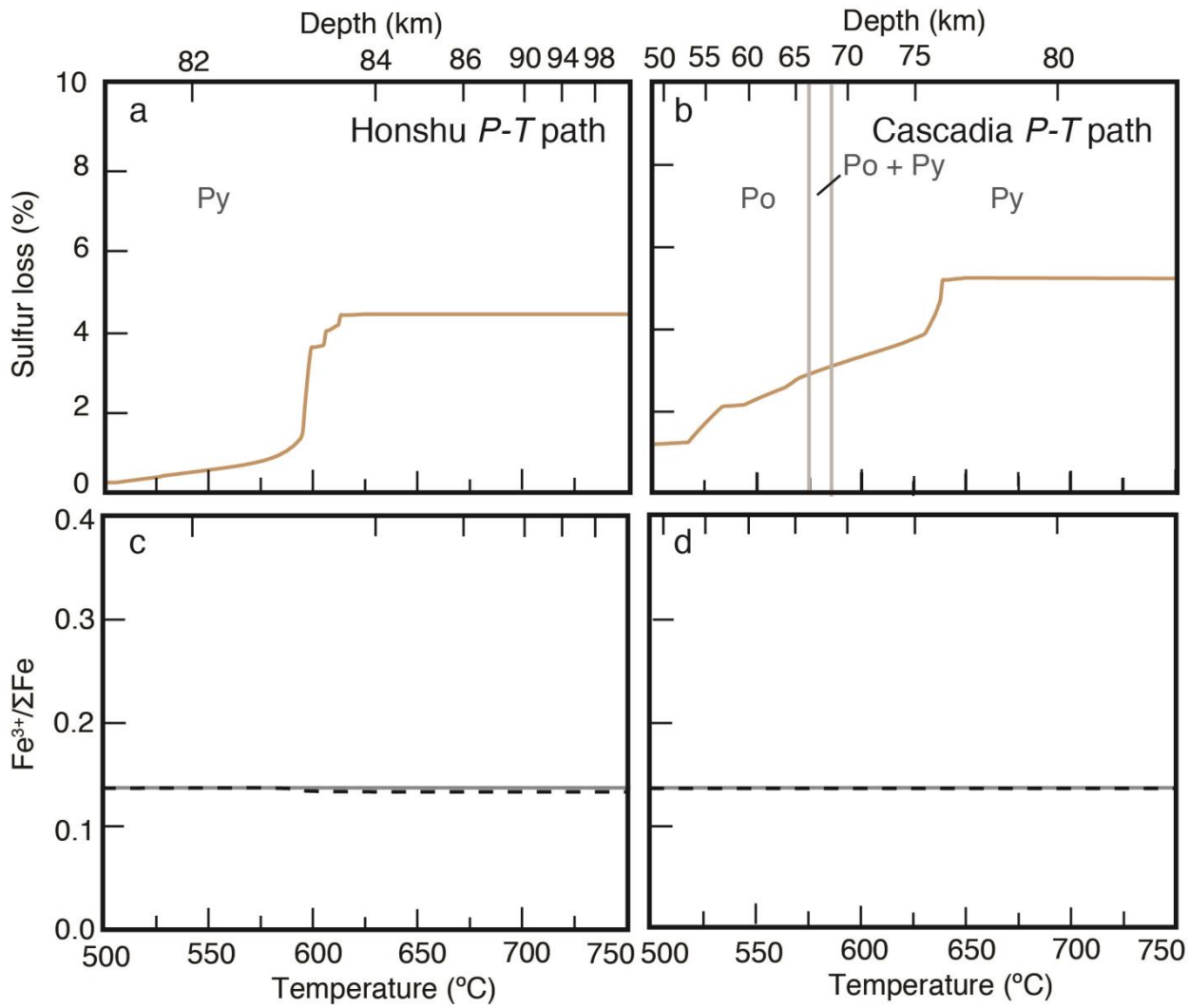

Figure S-10 Plots of percent sulfur loss **(**sulfur loss/initial sulfur concentration, **a-b)** and bulk rock $Fe^{3+}/\Sigma Fe$ **(c-d)** against temperature and depth along the Honshu and Cascadia *P–T* paths for an average MORB composition. Bulk rock $Fe^{3+}/\Sigma Fe$ ratio is plotted for both closed (solid grey) and open (dashed black) systems. Sulfide assemblages are also shown in grey. Only sulfides are stable over the *P–T* range of dehydration, as a result the $Fe^{3+}/\Sigma Fe$ remains nearly constant along both paths.

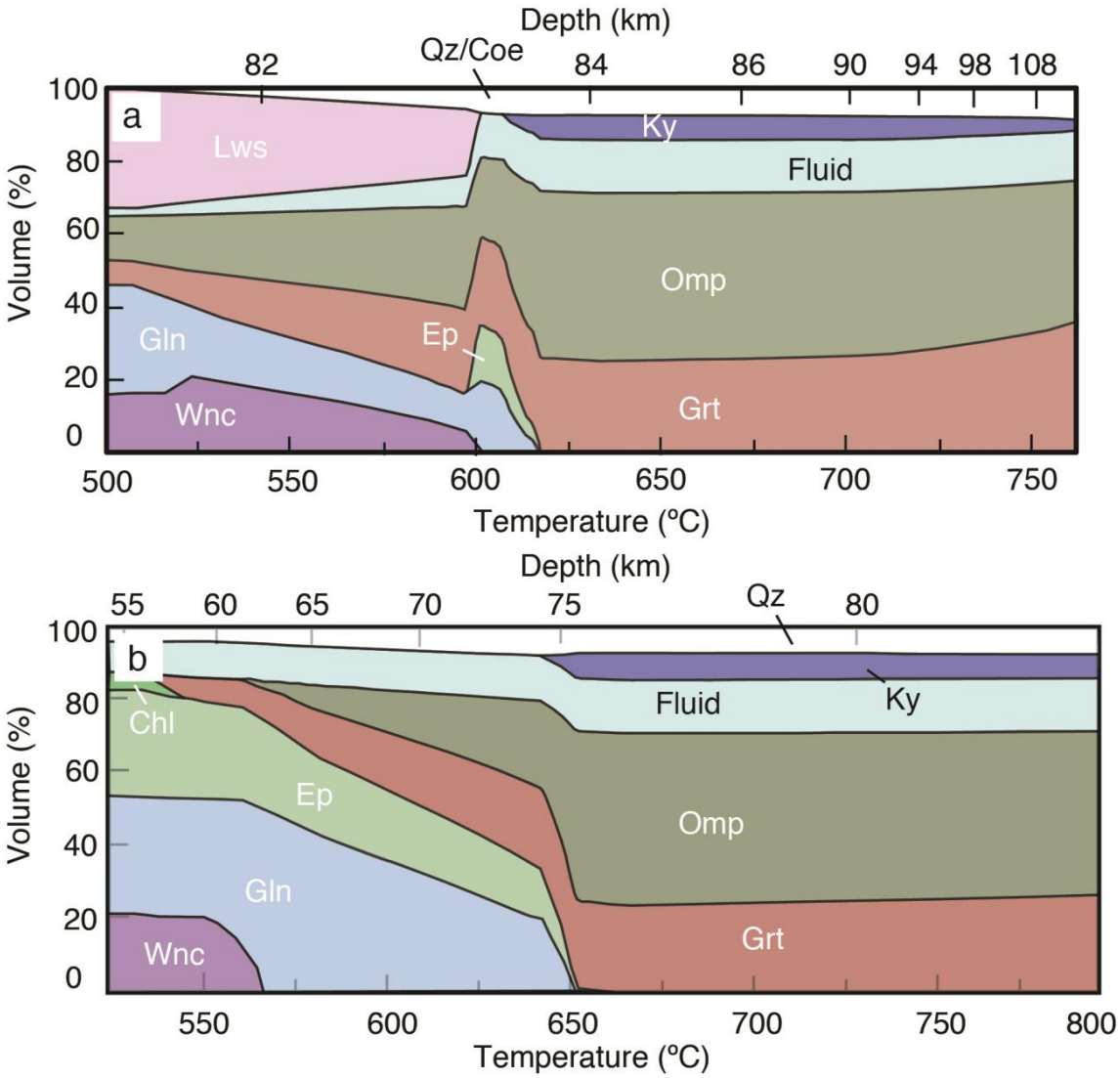

Figure S-11 Plots of major mineral abundances vs *T* and depth for **(a)** Honshu and **(b)** Cascadia *P*–*T* paths for the closed system MORB model. Sodic amphiboles are stabilised to higher *P*–*T* in for a MORB composition when compared to AOC. Sodic amphiboles are also more abundant than sodic-calcic amphiboles. Additionally, the epidote-out reaction occurs at lower *P*–*T* in the MORB models, resulting in shallower dehydration.

Supplementary Information References

Alt, J., Emmermann, R. (1985) Geochemistry of hydrothermally altered basalts: DSDP Hole 504B. *Initial Reports of the Deep Sea Drilling Project* 83, 249-262.

Alt, J., Anderson, T., Bonnell, L. (1989) The geochemistry of sulfur in a 1.3 km section of hydrothermally altered oceanic crust, DSDP Hole 504B. *Geochimica et Cosmochimica Acta* 53, 1011-1023.

Alt, J. (1995) Sulfur isotopic profile through the oceanic crust: Sulfur mobility and seawater-crustal exchange during hydrothermal alteration. *Geology* 23, 585-588.

Alt, J., Shanks, W.C. (2011) Microbial sulfate reduction and the sulfur budget for a complete section of altered oceanic basalts, IODP Hole 1256D (eastern Pacific). *Earth and Planetary Science Letters* 310, 73-83.

Bach, W., Edwards, K. (2003) Iron and sulfide oxidation within basaltic ocean crust: Implications for chemolithoautotrophic microbial biomass production. *Geochimica et Cosmochimica Acta Acta* 67, 3871-3887.

Birner, S.K., Cottrell, E., Warren, J.M., Kelley, K.A., Davis, F.A. (2018) Peridotites and basalts reveal broad congruence between two independent recorders of mantle fO_2 despite local redox heterogeneity. *Earth and Planetary Science Letters* 494, 172-189.

Blatter, D.L., Carmichael, I.S. (1998). Hornblende peridotite xenoliths from central Mexico reveal the highly oxidized nature of subarc mantle. Geology 26, 1035-1038.

Brandon, A.D., Draper, D.S. (1996). Constraints of the origin of the oxidation state of mantle overlying subduction zones: An example from Simcoe, Washington, USA. Geochimica et Cosmochimica Acta, 60, 1739-1749.

Connolly, J. (2005) Computation of phase equilibria by linear programming: a tool for geodynamic modeling and its application to subduction zone decarbonation. *Earth and Planetary Science Letters* 236**,** 524-541.

Connolly, J., Galvez, M. (2018) Electrolytic fluid speciation by Gibbs energy minimization and implications for subduction zone mass transfer. *Earth and Planetary Science Letters* 501, 90-102.

Coleman, R.G., Lee, D.E., Beatty. L.B., Brannock, W.W. (1965) Eclogites and eclogites: Their differences and similarities. *GSA Bulletin* 76, 483-508.

Connolly, J.A.D. (2005) Computation of phase equilibria by linear programming: a tool for geodynamic modelling and its application to subduction zone decarbonation. *Earth and Planetary Science Letters* 236, 524-541.

Cottrell, E., Kelley, K. (2011) The oxidation state of Fe in MORB glasses and the oxygen fugacity of the upper mantle. *Earth and Planetary Science Letters* 305, 270-282.

Emmermann, R. (1985) Basement geochemistry, Hole 504B. *Initial Reports of the Deep Sea Drilling Project* 83, 183-100.

Enders, M., Speer, D., Maresch, W.V., McCammon, C.A. (2000) Ferric/ferrous iron ratios in sodic amphiboles: Mössbauer analysis, stoichiometry-based model calculations and the high-resolution microanalytical flank method. *Contributions to Mineralogy and Petrology* 140, 135-147.

Ernst, W.G., Seki, Y., Onuki, H., Gilbert, M.C. (1970) Comparative study of low-grade metamorphism in the California Coast Ranges and the Outer Metamorphic Belt of Japan. *GSA Memoirs* 124, 1-274.

Ernst, W.G., Wai, C.M. (1970) Mössbauer, infrared, X-ray and optical study of cation ordering and dehydrogenation in natural and heat-treated sodic amphiboles. *American Mineralogist* 55, 1226-1258.

Evans, K.A., Powell, R., Holland, T.J.B. (2010) Internally consistent data for sulfur-bearing phases and application to the construction of pseudosections for mafic greenschist facies rocks in Na_2O-CaO-K_2O-FeO-MgO-Al_2O_3-SiO_2-CO_2-O-S-H_2O. *Journal of Metamorphic Geology* 28, 667-687.

Fisher, A.T. (2005) Marine hydrogeology: Future prospects for major advances. *Hydrogeology Journal* 13, 69-97.

Galvez, M.E., Beyssac, O., Martinez, I., Benzerara, K., Chaduteau, C., Malvoisin, B., Malavieille, J. (2013). Graphite formation by carbonate reduction during subduction. *Nature Geoscience* 6, 473-477.

Gerya, T.V., Stöckhert, B., Perchuk, A.L. (2002). Exhumation of high-pressure metamorphic rocks in a subduction channel: A numerical simulation. *Tectonic*s 21, 1-16.

Green, E.C.R., Holland, T.J.B, Powell, R. (2007) An order-disorder model for omphacitic pyroxenes in the system jadeite-diopside-hedenbergite-acmite, with applications to eclogitic rocks. *American Mineralogist*. 92, 1181-1189.

Green, E.C.R., White, R.W., Diener, J.F.A., Powell, R., Holland, T.J.B., Palin, R.M. (2016) Activity-composition relations for the calculation of partial melting equilibria in metabasic rocks. *Journal of Metamorphic Geology* 34, 845-869.

Hacker, B.R. (2008). H2O subduction beyond arcs. *Geochemistry, Geophysics,* Geosystems 9, Q03001.

Holland, T.J.B., Powell, R. (2011) An improved and extended internally consistent thermodynamic dataset for phases of petrological interest, involving a new equation of state for solids. *Journal of Metamorphic Geology* 29, 333-383.

Honnorez, J., Laverne, C., Hubberten, H.W., Emmermann, R., Muehlenbachs, K. (1983) Alteration processes in Layer 2 basalts, DSDP Hole 504B, Costa Rica Rift. *Initial Reports of the Deep Sea Drilling Project* 69-70, 509-546.

Hubberten, H.W., Emmermann, R., Puchelt, H. (1983) Geochemistry of basalts from Costa Rica Rife sites 504 and 505 (DSDP legs 69 and 70). *Initial Reports of the Deep Sea Drilling Project* 69-70, 629-635.

Li, Y.L., Zheng, Y.F., Fu, B. (2005) Mössbauer spectroscopy of omphacite and garnet pairs from eclogites: Application to geothermobarometry. *American Mineralogist* 90, 90-100.

Malaspina, N., Poli, S., Fumagalli, P. (2009). The oxidation state of metasomatized mantle wedge: Insights from C-O-H-bearing garnet peridotite. *Journal of Petrology* 50, 1533-1552.

Malaspina, N., Scambelluri, M., Poli, S., Van Roermund, H.L.M., Langenhorst, F. (2010). The oxidation state of mantle wedge majoritic garnet websterites metasomatized by C-bearing subduction fluids. *Earth and Planetary Science Letters* 298, 417-426.

Malaspina, N., Langenhorst, F., Fumagalli, P., Tumiati, S., Poli, S. (2012). Fe^{3+} distribution between garnet and pyroxenes in mantle wedge carbonate-bearing garnet peridotites (Sulu, China) and implications for their oxidation state. *Lithos* 146-147, 11-17.

Masci, L., Dubacq, B., Verlaguet, A., Chopin, C., De Andrade, V., Herviou, C. (2019) A XANES and EPMA study of Fe^{3+} in chlorite: Importance of oxychlorite and implications for cation site distribution and thermobarometry. *American Mineralogist* 104, 403-417.

Mungall, J.E. (2002) Roasting the mantle: Slab melting and the genesis of major Au and Au-rich Cu deposits. *Geology* 30, 915-918.

Parkinson, I.J., Arculus, R.J., Eggins, S.M. (2003). Peridotite xenoliths from Grenada, Lesser Antilles Island Arc. *Contributions to Mineralogy and Petrology* 146, 241-262.

Peslier, A., Luhr, J., Post, J. (2002). Low water contents in pyroxenes from spinel-peridotites of the oxidized, sub-arc mantle wedge. *Earth and Planetary Science Letters* 201, 69-86.

Proyer, A., Dachs, E., McCammon, C. (2004) Pitfalls in geothermobarometry of eclogites: Fe^{3+} and changes in the mineral chemistry of omphacite at ultrahigh pressures. *Contribributions to Mineralogy and Petrology* 147, 305-318.

Schmid, R., Wilke, M., Oberhänsli, R., Janssens, K., Falkenberg, G., Franz, L., Gaab, A. (2003) Micro-XANES determination of ferric iron and its application in thermobarometry. *Lithos* 70, 381-392.

Sverjensky, D.A., Harrison, B., Azzolini, D. (2014) Water in the deep Earth: the dielectric constant and the solubilities of quartz and corundum to 60 kb and 1200 degrees C. *Geochimica et Cosmochimica Acta* 129, 125-145.

Syracuse, E.M., van Keken, P.E., Abers, G.A. (2010) The global range of subduction zone thermal models. *Physics of the Earth and Planetary Interiors* 183, 73-90.

Tomkins, A.G., Evans, K.A. (2015). Separate zones of sulfate and sulfide release from subducted mafic oceanic crust. *Earth and Planetary Science Letters* 428, 2015.

Tumiati, S., Malaspina, N. (2019). Redox processes and the role of carbon-bearing volatiles from the slab-mantle interface to the mantle wedge. *Journal of the Geological Society* 176, 388-397.

Vitale Brovarone, A., Martinez, I., Elmaleh, A., Compagnoni, R., Chadutea, C., Ferraris, C., Esteve, I. (2017). Massive production of abiotic methane during subduction evidenced in metamorphosed ophicarbonates from the Italian Alps. *Nature Communications* 8, 14134.

Van Keken, P.E., Hacker, B.R., Syracuse, E.M., Abers, G.A. (2011). Subduction factory: 4. Depth-dependent flux of H2O from subducting slabs worldwide. *Journal of Geophysical Research* 116, B01401.

White, R.W., Powell, R., Holland, T.J.B. (2007) Progress relating to calculation of partial melting equilibria for metapelites. *Journal of Metamorphic Geology* 25, 511-527.

White, R.W., Powell, R., Johnson, T.E. (2014) The effect of Mn on mineral stability in metapelites revisted: new a-x relations for manganese-bearing minerals. *Journal of Metamorphic Geology* 32, 809-828.

Whitney, D.L., Evans, B. (2010) Abbreviations for names of rock-forming minerals. *American Mineralogist* 95, 185-187.